

Analysis Note

Directed flow v_1 of protons in the Xe+Cs(I) collisions at 3.8 AGeV

Mikhail Mamamev¹, Arkadiy Taranenko², Alexander Demanov, Petr Parfenov,
Valery Troshin.

National Research Nuclear University MEPhI, Moscow, Russia
Joint Institute for Nuclear Research, Dubna, Russia

In this note, we present the directed flow v_1 measurements of protons from Xe+Cs(I) collisions at 3.8 AGeV (BM@N run8). We show the datasets, event and track selection cuts, centrality definition, event plane reconstruction and resolution. The v_1 results are presented as function of transverse momentum (p_T) and rapidity (y_{cm}) for 10-30% central Xe+Cs(I) collisions. The systematic uncertainty study will also be presented and discussed. The v_1 measurements are compared with results of JAM transport model calculations and published data from other experiments.

The work has been supported by the Ministry of Science and Higher Education of the Russian Federation, Project “Fundamental and applied research at the NICA megascience experimental complex” № FSWU-2024-0024.

¹E-mail: mam.mih.val@gmail.com

²E-mail: AVTaranenko@mephi.ru

Contents

1	Introduction	2
2	Directed and elliptic flow of protons	5
3	Analysis details	9
3.1	The layout of the BM@N experiment	9
3.2	Quality Assurance (QA) study	11
3.3	Data, Event and Track Selection	20
3.4	Centrality determination	24
4	Methods for analyzing anisotropic flow in BM@N	30
4.1	General framework for the flow measurements	30
4.2	BM@N performance for flow measurements	37
4.3	The analysis of v_1 of protons from BM@N run8 data	42
4.4	Systematic uncertainties of v_1 measurements	45
5	Results of the directed flow measurements	47

1 Introduction

Relativistic heavy-ion collisions can directly generate the high density and/or temperature strong interacting matter, and thus provide the opportunity to explore the strong interaction properties at extreme conditions. One of the interests is the exploration of nuclear Equation of State (EoS) as well as the symmetry energy for asymmetric nuclear matter at high densities [1]. The anisotropic collective flow of final state particles is a direct reflection of the pressure and its gradients created in relativistic heavy-ion collisions and thus is closely related to the EoS of dense matter. The anisotropic flow can be quantified by Fourier coefficients v_n [2–5] in the expansion of the particle azimuthal distribution relative to the reaction plane given

by the angle Ψ_R :

$$dN/d\phi \propto 1 + \sum_{n=1} 2v_n \cos(n(\varphi - \Psi_R)), \quad (1)$$

where n is the order of the harmonic and φ is the azimuthal angle of a particle of the given type. The flow coefficients v_n can be calculated as $v_n = \langle \cos[n(\varphi - \Psi_R)] \rangle$, where the brackets denote the average over the particles and events. The directed (v_1) and elliptic (v_2) flows are dominant and most studied signals in the energy range of $2 < \sqrt{s_{NN}} < 5$ GeV [6–12]. The comparison of existing measurements of v_1 and v_2 of protons and light fragments in Au+Au collisions at $\sqrt{s_{NN}} = 2.07$ -4.72 GeV (corresponding to beam energies $E_{beam} = 0.4$ -10 AGeV) with results from hadronic transport simulations provides the most stringent currently available constraints on the high-density EOS of symmetric nuclear matter [1; 13; 14], see the right panel of Figure 1. At densities between 1 and 2 times saturation density ρ_0 , the v_2 data for protons, deuterons and tritons in Au+Au collisions measured at $E_{beam} = 0.4$ -1.49 AGeV ($\sqrt{s_{NN}} = 2.07$ -2.51 GeV) by the FOPI experiment at GSI [9] have been used together with IQMD model transport calculations to constrain the nuclear incompressibility K_{nm} [15]. The model that takes into account momentum-dependent interactions, can explain the data with a fairly soft EOS ($K_{nm} = 190 \pm 30$ MeV) [14], see the solid yellow region in the right panel of Figure 1.

At densities ~ 2 -5 ρ/ρ_0 , the comparison of the existing v_1 and v_2 measurements of protons in Au+Au at $E_{beam} = 2$ -8 AGeV ($2.5 < \sqrt{s_{NN}} < 4.5$ GeV) by the E895 experiment at AGS [6–8] with results of microscopic transport models leads to the values of nuclear incompressibility $K_{nm} = 200$ -380 MeV [13], depicted by the grey hatched region in Figure 1. The description of v_1 results from E895 experiment requires a soft EOS with the incompressibility $K_{nm} = 200$ MeV, while reproducing the v_2 data required larger values of $K_{nm} = 380$ MeV (and therefore a harder EOS). A Bayesian analysis study [16] suggests a difference between the E895 [6–8] and recently obtained STAR [11; 12] data from RHIC Beam Energy Scan program. Using only the STAR measurements, the study [16] further found that the slope of the directed flow and the elliptic flow of protons can be described by the transport model with the same EOS. The E895 flow measurements [6–8] have been performed 15-20 years ago

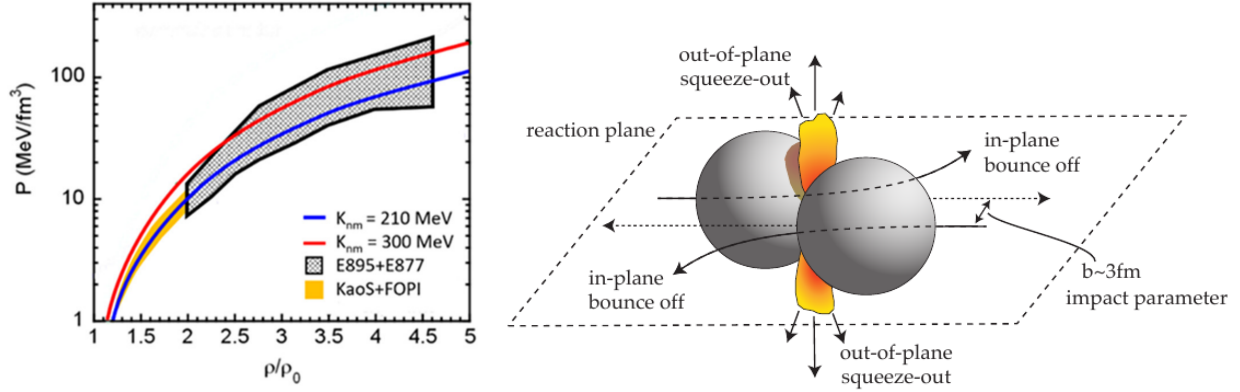


Figure 1: Left panel: Pressure as function of baryon density for symmetric nuclear matter. Selected constraints on the symmetric EOS obtained from comparisons of experimental flow data to hadronic transport simulations, see text for the details. The figure is taken from [14]. Right panel: Illustration of a semi-central collision of two nuclei with an impact in the $\sqrt{s_{NN}} = 2.0\text{-}3.5$ GeV energy regime, with the direction of the flow phenomena indicated with arrows into ($v_1 > 0$ or “bounce-off” of spectators) or perpendicular ($v_2 < 0$ or “squeeze-out”) to the reaction plane.

by the standart event plane method, which do not take into account the influence of non-flow effects on v_n measurements [17]. Therefore, high-precision measurements of anisotropic flow at $2 < \sqrt{s_{NN}} < 5$ GeV with a modern methods of analysis are required, in order to further constrain the EOS of symmetric matter from model comparisons [14; 17].

The important characteristic of this energy range is that the compressed overlap zone expands at the time t_{exp} comparable to the passage time t_{pass} , at which the accelerated nuclei interpenetrate each other. The expansion time $t_{exp} \sim R/c_s$ is governed by a fundamental property, the speed of sound c_s which connects to the EOS [8; 13]. The passage time t_{pass} can be estimated as $t_{pass} = 2R/\sinh(y_{beam})$, where R is the radius of the nucleus and y_{beam} is the beam rapidity [7; 8; 13]. For Au+Au collisions at $2.4 < \sqrt{s_{NN}} < 5$ GeV, the t_{pass} decreases from 18 fm/c to 6 fm/c. If the passage time is long compared to the expansion time, spectator nucleons serve to block the path of produced hadrons emitted towards the reaction plane. Such rather complex collision geometries result in strong change in the resulting flow patterns. For example, for Au+Au collisions at $\sqrt{s_{NN}} < 3.3\text{-}3.5$ GeV, the nuclear matter is “squeezed-out” perpendicular to the reaction plane giving rise to negative elliptic flow

($v_2 < 0$) and squeeze-out contribution should then reflect the ratio $c_s/\sinh(y_{beam})$ [8; 13], see the right panel of Figure 1. The t_{pass} depends on the size of colliding system and beam energy. Therefore, the study of the system size dependence of anisotropic flow may help to estimate the participant-spectator contribution and improve our knowledge of EOS of symmetric nuclear matter.

The Baryonic Matter at the Nuclotron (BM@N)[18] is a fixed target experiment at JINR (Dubna), In February 2023, the first physics run of the BMN experiment was completed with recorded Xe + Cs(I) collision events at $E_{beam} = 3$ AGeV ($\sqrt{s_{NN}} = 3.02$ GeV) and 3.8 AGeV ($\sqrt{s_{NN}} = 3.26$ GeV). In this analysis note, we present first results on directed flow (v_1) of protons in 10-30% central Xe + Cs(I) collisions at $E_{beam} = 3.8$ AGeV. The note is organized as follows. Section 2 briefly discusses the existing data on flow of protons and transport model predictions. Section 3 introduces the BM@N experimental set-up, QA study, the centrality and the particle identification methods, while section 4 discusses the procedures used to determine the flow coefficients and systematic uncertainty study. Section 5 presents the main results on directed flow v_1 of protons.

2 Directed and elliptic flow of protons

A large amount of data on measurements of directed v_1 and elliptic v_2 flow of protons in nucleus-nucleus collisions in the energy region of $\sqrt{s_{NN}} = 2.4-5.0$ GeV has been accumulated over the past 20 years [6–12; 19]. At the moment, the main source of new experimental v_n data is the analysis of Au + Au collision events, which were collected by the STAR experiment as part of the Beam Energy Scan II program at RHIC [12; 19; 20], see Figure 2 as an example. The main results of measurements of v_1 and v_2 of protons can be summarized as follows:

1): The relatively long passing time t_{pass} leads to the interaction of particles with spectator nucleons, which flow predominantly in the reaction plane. For Au+Au collisions at $2.4 < \sqrt{s_{NN}} < 5$ GeV, the t_{pass} decreases from 18 fm/c to 6 fm/c. As result the v_1 , the slope of the v_1 at mid-rapidity $dv_1/dy|_{y=0}$ and v_2 of protons decrease with increasing collision energy, see Figure 2. The v_2 signal is undergo the transition from $v_2 < 0$ (“out-of-plane”) to $v_2 > 0$ (“in-plane”) at $\sqrt{s_{NN}} \sim 3.3$ GeV [7; 20]. All

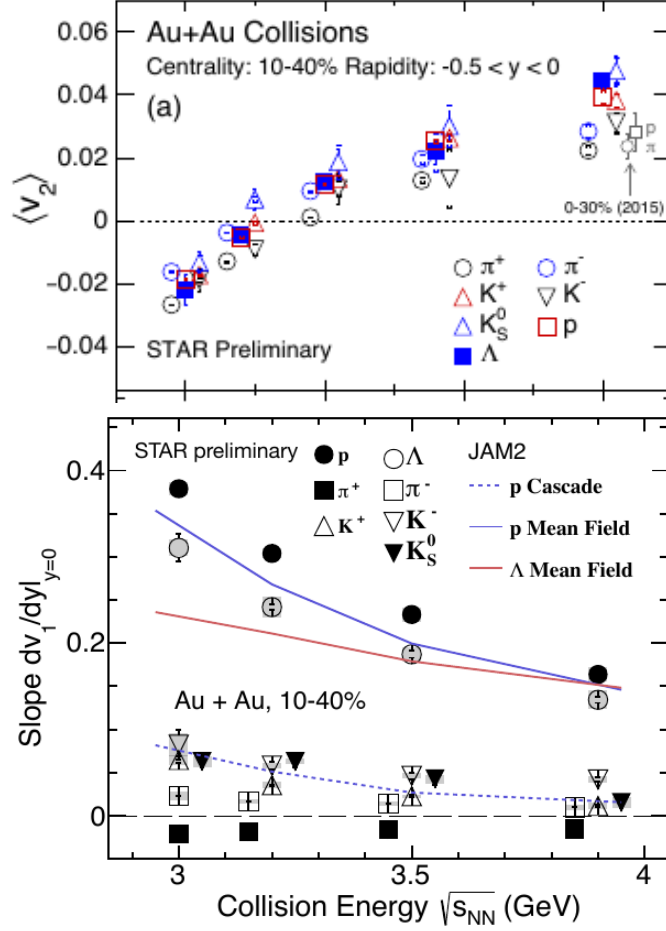


Figure 2: Elliptic flow v_2 (upper panel) and slope of the directed flow at mid-rapidity $dv_1/dy|_{y=0}$ (low panel) for different particle species from 10-40% central Au+Au collisions at $\sqrt{s_{NN}}=3.0, 3.2, 3.5$ and 3.9 GeV from the STAR Beam Energy Scan II program [19; 20]

existing measurements of v_1 and v_2 of protons were performed with respect to the first-order event plane, which is determined by the directed flow v_1 of the spectator nucleons. It is the dominant flow signal in amplitude and does not change sign in this collision energy range.

2): While v_1 of protons is consistent with zero at mid-rapidity ($y_{cm}=0$), it rises towards forward and decreases towards backward rapidities (see left panel of Figure 3). The rapidity dependence v_2 is opposite to v_1 , i.e. the absolute value of v_2 is largest at mid-rapidity and decreases towards forward and backward rapidities, see right panel of Figure 3. The $v_1(p_T)$ of protons exhibits an almost linear rapid rise in the region $p_T < 0.6$ GeV/c and then increases only moderately or even saturates for $p_T > 1$ GeV/c, see [10] for plots. The v_2 values around mid-rapidity decrease (increase)

continuously with p_T for collision energies below (above) $\sqrt{s_{NN}} \simeq 3.3$ GeV.

3): The slope of v_1 of protons at mid-rapidity $dv_1/dy|_{y=0}$ exhibits no significant

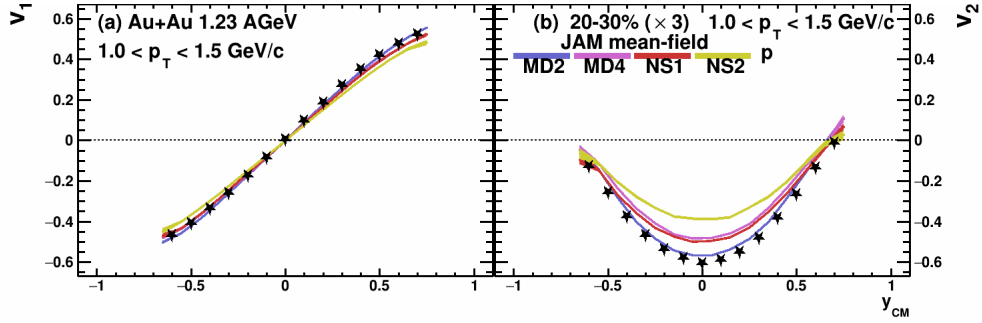


Figure 3: Rapidity (y_{cm}) dependence of v_1 (left) and v_2 (right) of protons with $1.0 < p_T < 1.5$ GeV/c in the 20-30% central Au+Au collisions at $\sqrt{s_{NN}} = 2.4$ GeV. The closed star symbols represent the published HADES data [10]. The blue (MD2), purple (MD4), red (NS1) and yellow (NS2) bands represent the results from the mean-field mode of the JAM model with different EOS, as indicated. The figure is taken from [21].

centrality dependence for all p_T intervals, except for the very central class where $dv_1/dy|_{y=0}$ is smaller than for the other centralities, see left panel of Figures 4 and upper panel of Figure 5. In contrast, the v_2 signal of protons has a strong (almost linear) dependence on centrality, see right panel of Figure 4 and lower panel of Figure 5. The fluctuations of v_1 and v_2 may lead to non-zero values in the most central collisions. The strong p_T and centrality dependence of v_2 can be explained in a simple way. A specific particle moving with transverse velocity v_t will be shadowed by the spectator matter during the passage time t_{pass} . The simple geometrical estimate then leads to the condition [22]: $v_t > (2R - b)/t_{pass}$, where R is the radius of the nucleus and b is the impact parameter. It is easier to fulfill this condition for the particle with high p_T and for peripheral collisions.

4): The detailed multi-differential study of flow coefficients v_n of protons in relativistic heavy-ion collisions at $\sqrt{s_{NN}} = 2.4$ -5.0 GeV using several hadronic transport models: UrQMD [23], PHQMD [24], DCM-QGSM-SMM [25], SMASH [1] and JAM [26–28] and comparison with published HADES/STAR proton flow data can be found in [1; 10; 12; 17; 21]. The cascade mode of all models (UrQMD, DCM-QGSM-SMM, SMASH, JAM) failed to describe the existing experimental flow data [21].

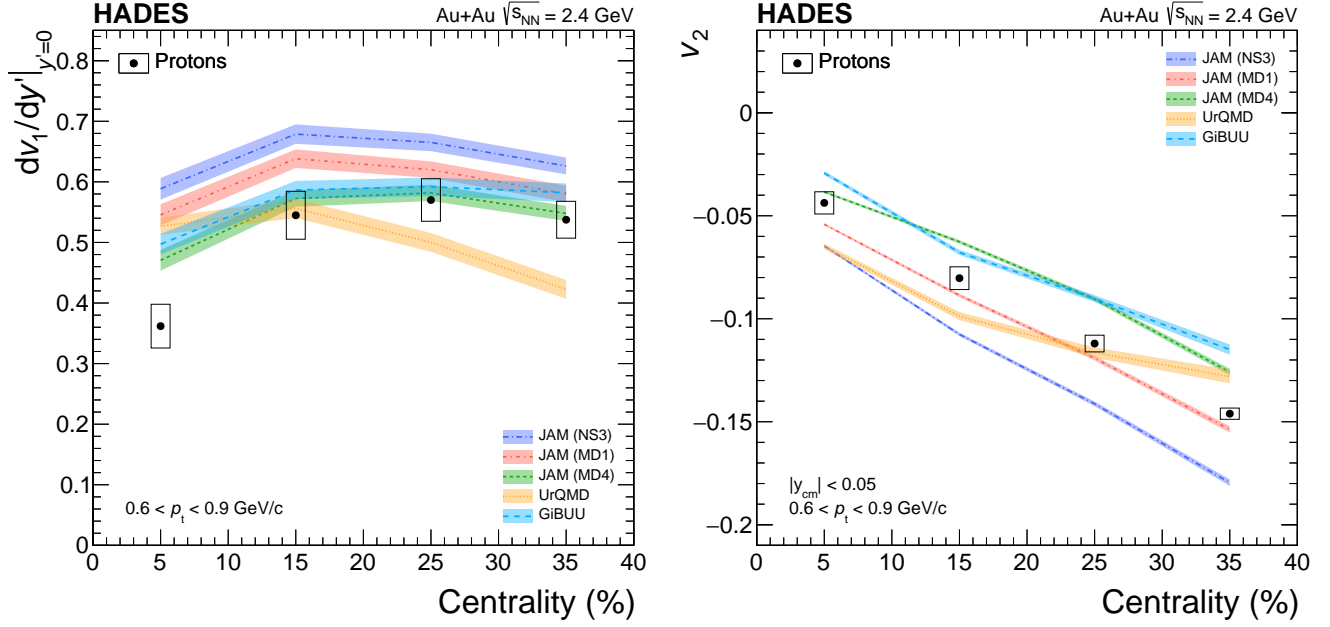


Figure 4: The slope $dv_1/dy'|_{y'=0}$ (left panel) and elliptic v_2 (right panel) flow of protons in the interval $0.6 < p_T < 0.9$ GeV/c at mid-rapidity in Au+Au collisions at $\sqrt{s_{NN}} = 2.4$ GeV for four centrality classes. The HADES data are compared to several model predictions. The figure is taken from [10]

The absence of a repulsive potential significantly reduces the v_1 and v_2 signals and results in essentially zero signals for the higher order (v_3 and v_4) flow coefficients for protons. However, by including the meanfield potential, the JAM and UrQMD models can qualitatively reproduce the HADES and STAR data for p_T and rapidity (y_{cm}) dependence of anisotropic flow coefficients v_1 and v_2 of protons in Au+Au collisions at $\sqrt{s_{NN}} = 2.4$ and 3.0 GeV[1; 10; 12; 17; 21]. In the present work, we use the Jet AA Microscopic transport model (JAM) [26–28] as the main event generator to simulate Xe+Cs(I) collisions for anticipated performance of the BM@N spectrometer for flow measurements of protons and for the comparison with first v_1 data. The nuclear mean field is simulated based on the relativistic version of the QMD model (RQMD.RMF)[28]. We have used the version JAM 1.9092 which includes five different EOS implementations, see [17; 21] for details.

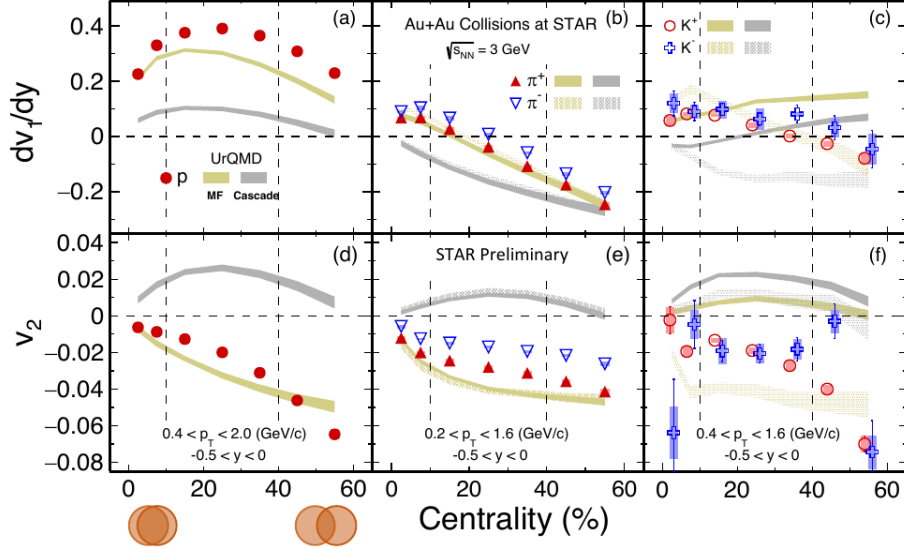


Figure 5: The centrality dependence of the slope $dv_1/dy|_{y=0}$ (upper panel) and elliptic v_2 (lower panel) flow of protons, pions and kaons at mid-rapidity in Au+Au collisions at $\sqrt{s_{NN}} = 3.0$ GeV. The STAR data are compared to UrQMD model prediction. The figure is taken from [12; 19]

3 Analysis details

This section briefs about the related details for analysis of the experimental data for Xe+Cs(I) collisions at 3.8 AGeV (BM@N run8), such as the selection of good events and tracks for analysis, particle identification used for selecting protons, and the definition of collision centrality for geometry of collisions. Prior to conducting physical analysis, the data underwent a thorough evaluation to ensure that only good runs were included, called run-by-run Quality Assurance (QA).

3.1 The layout of the BM@N experiment

The BM@N detector is a forward spectrometer that covers the pseudorapidity range $1.6 \leq \eta \leq 4.4$ [18]. The layout of the BM@N experiment for the Xe+Cs(I) run8 is shown in the Figure 6. The main subsystems of the BM@N [18] are the tracking system for charged hadron tracking, the Time Of Flight (TOF) system for charged particle identification and the set of forward detectors for centrality and reaction plane estimations. The tracking system is comprised of 4 stations of the Forward Silicon Detector (FSD) and 7 stations of Gaseous Electron Multipliers

(GEM) chambers mounted downstream of the silicon sensors, see left part of Figure 6. Both the silicon tracking system (FSD) and the GEM stations will be operated in the magnetic field (at maximum value of 1.2 T) of a large aperture dipole magnet and allow the reconstruction of the momentum p of charged particles. The z axis of the BM@N coordinate system is directed along the beam line, while the magnetic field is directed along the y axis. The FSD+GEM system provides also the measurements of the multiplicity of the produced charged particles N_{ch} , which can be used as an estimator of the collision centrality.

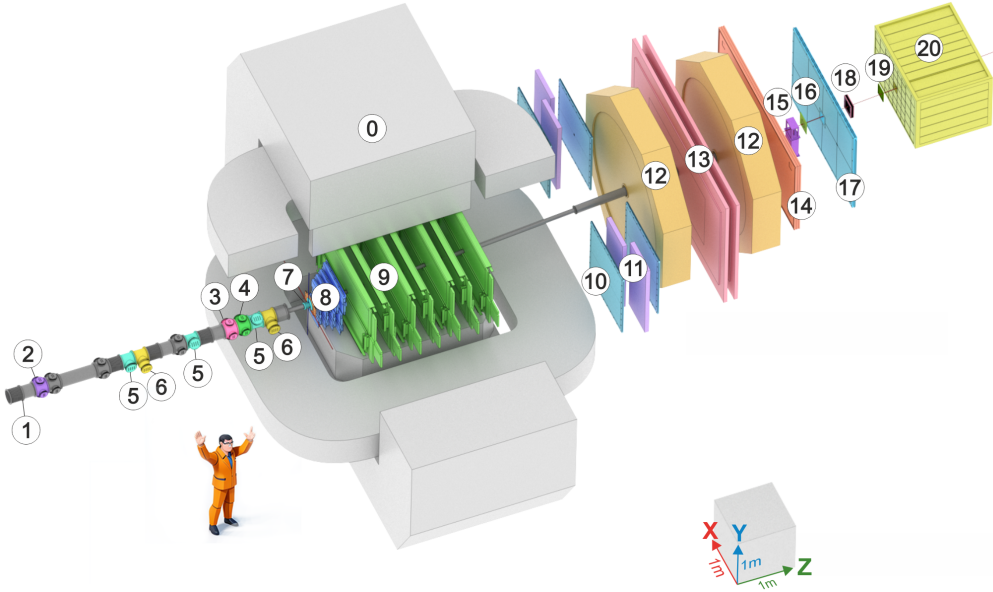


Figure 6: The layout of the BM@N experiment for the Xe+Cs(I) run8 2022-2023. Main components: (0) SP-41 analyzing magnet, (1) vacuum beam pipe, (2) BC1 beam counter, (3) Veto counter (VC), (4) BC2 beam counter, (5) Silicon Beam Tracker (SiBT), (6) Silicon beam profilometers, (7) Barrel Detector (BD) and Target station, (8) Forward Silicon Detector (FSD), (9) Gaseous Electron Multiplier (GEM) detectors, (10) Small cathode strip chambers (Small CSC), (11) TOF400 system, (12) drift chambers (DCH), (13) TOF700 system, (14) Scintillation Wall (ScWall), (15) Fragment Detector (FD), (16) Small GEM detector, (17) Large cathode strip chamber (Large CSC), (18) gas ionization chamber as beam profilometer, (19) Forward Quartz Hodoscope (FQH), (20) Forward Hadron Calorimeter (FHCAL). The figure is taken from [18]

The TOF-system consists of 3 planes of multi-gap Resistive Plate Chambers (mRPC) placed at $z = 400$ and $z = 700$ cm (TOF-400 and TOF-700, respectively) from the target, see the central part of Figure 6. The detectors BC1 and

BC2 define the start time for the time-of-flight system. Three forward detectors: Forward Hadronic Calorimeter (FHCAL), quartz hodoscope (Hodo) and Scintillator Wall (ScWall) provide the information about the spectator fragments, see the right part of the Figure 6. FHCAL provides the information about the energy of spectators fragments and consists of 54 modules. The modules have sampling structure and consist of a set of lead and scintillator plates compressed together by a steel band. FHCAL has a $15 \times 15 \text{ cm}^2$ square beam hole in the center. The beam hole leads to the leakage of the fragments with small transverse momenta. As a result, the deposited energy in the FHCAL is comparable for the central and peripheral events. This creates an ambiguity in the dependence of energy deposition on the collision centrality. New forward quartz hodoscope (Hodo) has been developed to be placed in the beam hole to measure the energy of spectator fragments. It helps to compensate the effect due to the leakage of the heavy fragments mostly in the peripheral collisions. ScWall has a wider acceptance than FHCAL and provides information about the charge of spectator fragments.

3.2 Quality Assurance (QA) study

The collection of events for a collision energy is done over several discrete time spans. Each of these time spans where the detector was continuously recording events is called a "run" and it can be selected by RunId. Each run consists of event and track information of the heavy-ion collisions recorded by the BM@N detector. We perform quality assurance (QA) checks for the selection of good runs. Averaged QA observables like: N_{ch} (charged particle multiplicity in FSD+GEM system), E_{tot} (total energy of spectator fragments in the FHCAL), N_{vtx} (number of tracks in the vertex reconstruction), etc., are calculated for each run. Then, the mean (μ) and standard deviation (σ) are calculated for the distribution of selected observables Y as a function of RunId:

$$\mu = \frac{1}{N} \sum_{i=1}^N Y_i \quad (2)$$

$$\sigma = \sqrt{\frac{1}{N} \sum_{i=1}^N (Y_i - \mu)^2}, \quad (3)$$

where i - RunId number and N - total numbers of runs. The runs for which the averaged QA observables lie beyond $\pm 3\sigma$ away from their global means are identified as bad runs, and all the events from that run are removed from the analysis.

Converter (DST to QA tree): <https://github.com/DemanovAE/convertBmn.git>

QA code: https://github.com/DemanovAE/QA_bmn.git

DST run8 data: /eos/nica/bmn/exp/dst/run8/24.04.0 (May 2024)

QA Data .tree.root at Clusters

NICA: /nica/mpd1/demanov/data_bmn/run8_vf_24.04.0

HybriLIT: /lustre/home/user/a/ademanov/bmn/data/run8_vf_24.04.0

Several examples of the application of the QA checks for different BM@N observables which provide the event and track information can be found below.

- 1) Figures 7–8 show the RunId dependence of the mean number of FSD, GEM, TOF400 and TOF700 digits. Black dotted horizontal line and red horizontal lines represent μ and $\pm 3\sigma$, respectively.
- 2) Figure 9 shows the RunId dependence of the mean number of tracks used in the vertex reconstruction. Figure 10 shows the RunId dependence of the mean x, y and z positions of the reconstructed vertex.
- 3) Figure 11 shows the RunId dependence of the mean multiplicity of charged particles in the tracking system (FSD + GEM)

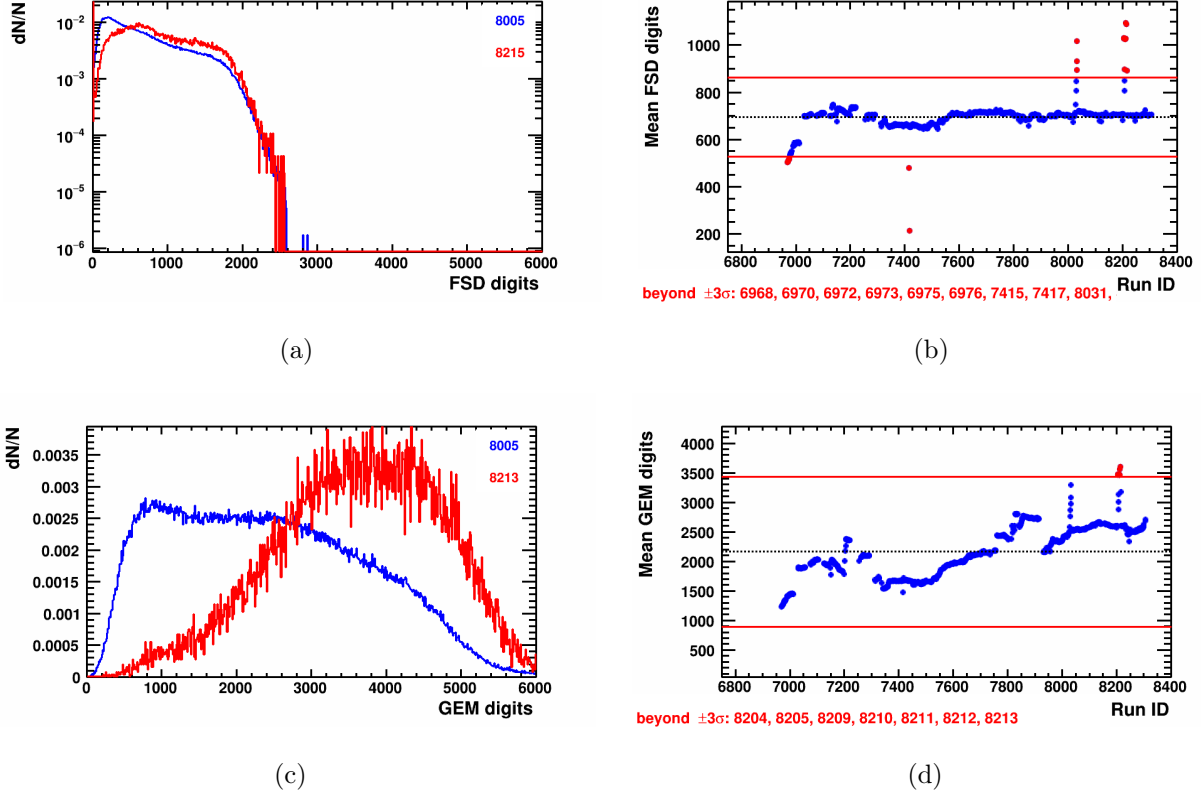


Figure 7: Distribution of the number of digits in the FSD (a) and GEM (c) detectors. The red marker corresponds to the distribution from the "outlier" RunId. Mean number of FSD digits (b) and GEM digits (d) as a function of RunID (right panel). Black dotted horizontal line and red horizontal lines represent μ and $\pm 3\sigma$, respectively.

4) Figures 12–13 shows the RunId dependence of the mean of the total energy E_{tot} of spectator fragments in the FHCAL and mean of the charge (Q^2) of spectator fragments in the forward quartz hodoscope (FQH). Black dotted horizontal line and red horizontal lines represent μ and $\pm 3\sigma$, respectively.

5) Figure 14 shows the RunId dependence of the mean of x, y and z components of the momentum of the charged particles. The upper panels of Figure 15 show the typical distributions of the transverse momentum p_T (left), azimuthal angle ϕ (center) and pseudorapidity η (right) of charged particles. Bottom panels of Figure 15 show the RunId dependence of the mean p_T , ϕ and η distributions. Figure 16 shows the correlations between the η and ϕ (left), η and p_T (center), ϕ and p_T (right) for charged particles. The upper panels of Figure 17 show the typical distributions for

the number of nHits to accurate the track momentum reconstruction (left) and the distance of closest approach DCA_R (right). The bottom panels show the RunId dependence of the mean nHits and DCA_R .

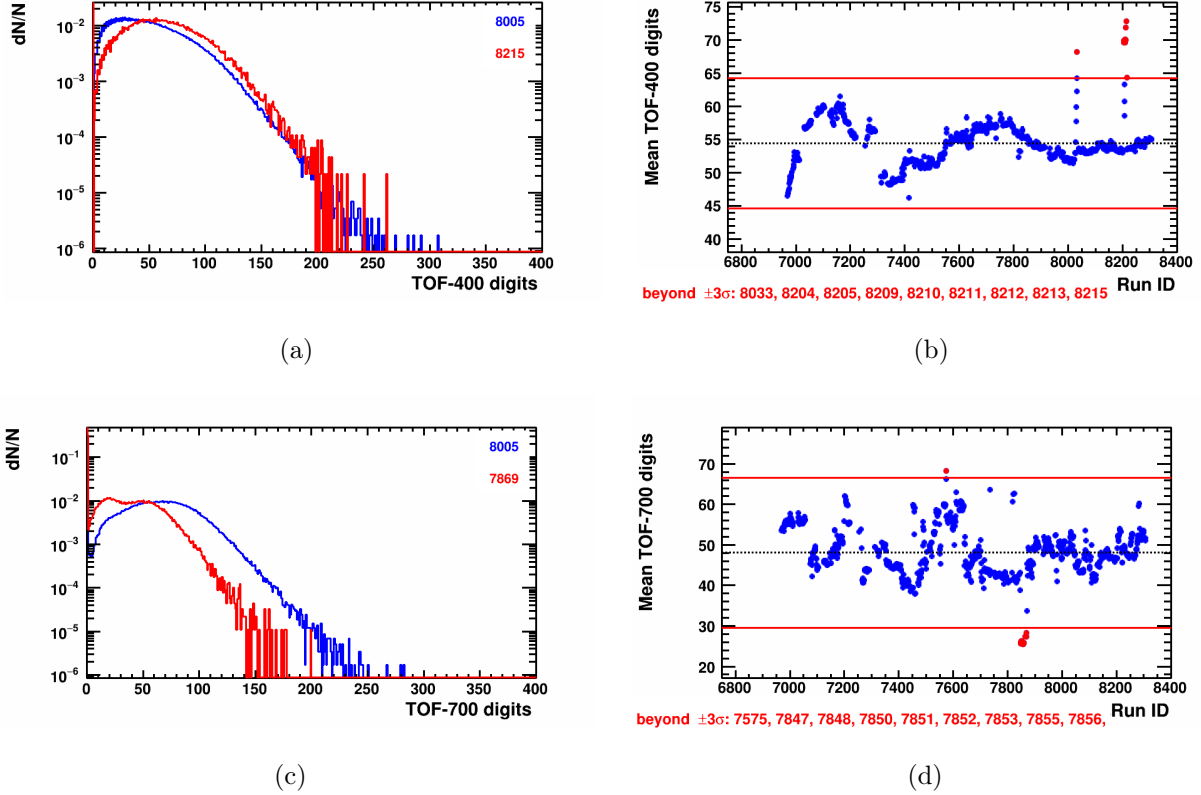


Figure 8: Distribution of the number of digits in the TOF400 (a) and TOF700 (c) detectors. The red marker corresponds to the distribution from the "outlier" RunId. Mean number of TOF400 digits (b) and TOF700 digits (d) as a function of RunID (right panel). Black dotted horizontal line and red horizontal lines represent μ and $\pm 3\sigma$, respectively.

6) As an example, the Figure 18 shows the population of all charged particles in the plane spanned by their mass squared (m^2) vs. laboratory momentum divided by charge (rigidity) for the TOF-400 (left panel) and TOF-700 (right panel) detectors. The left panels of Figure 19 show the distributions of the mass squared (m^2) and Gaussian fit of the proton peak for the TOF-400 (left upper panel) and TOF-700 (left bottom panel) detectors. Center and right panels of Figure 19 show the RunID dependence of mean of the mass squared (m^2) of proton and the width of the peak σ_{m^2} .

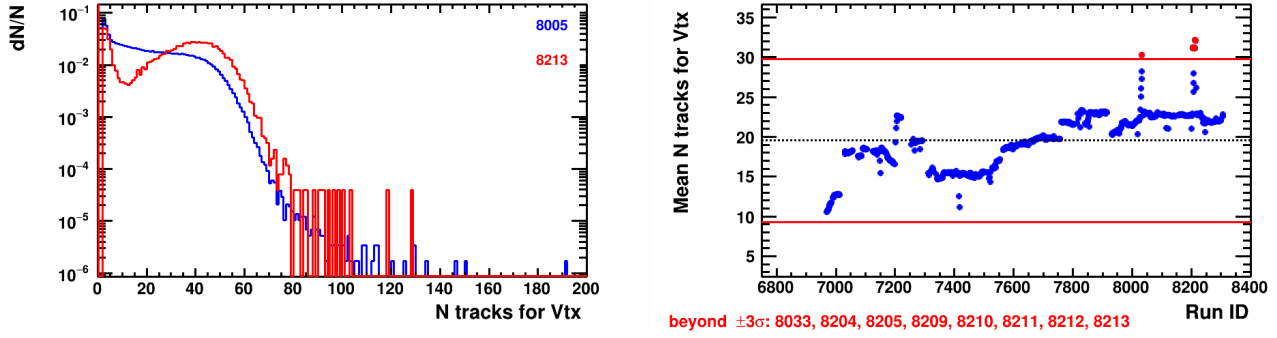


Figure 9: Left panel: distribution of the number of tracks in the vertex reconstruction. The red marker corresponds to the distribution from the "outlier" RunID. Right panel: Mean the number of tracks in vertex reconstruction as a function of RunID. Black dotted horizontal line and red horizontal lines represent μ and $\pm 3\sigma$, respectively.

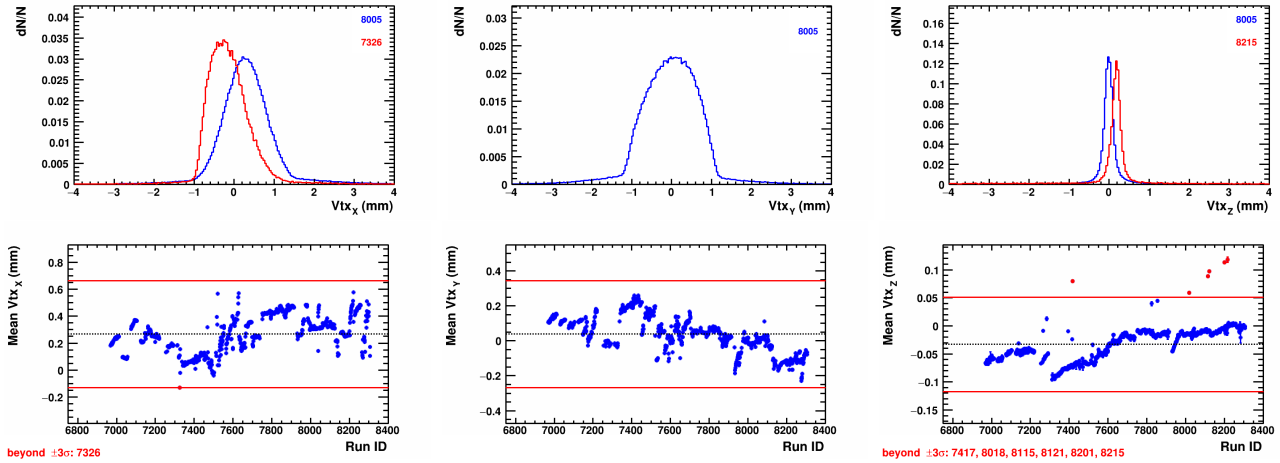


Figure 10: Upper panels: distribution of the x, y and z positions of vertex. The red marker corresponds to the distribution from the "outlier" RunID. Bottom panels: Mean of the x, y and z positions of the vertex as a function of RunID. Black dotted horizontal line and red horizontal lines represent μ and $\pm 3\sigma$, respectively.

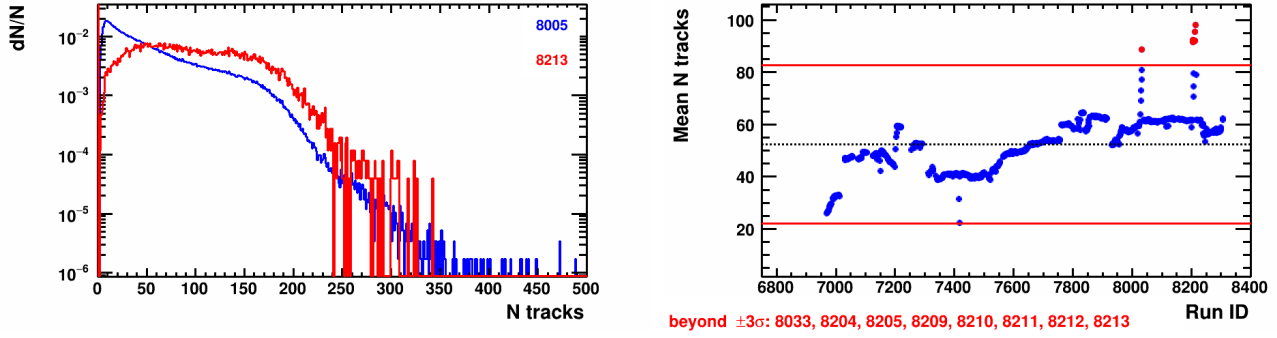


Figure 11: Upper panels: Distribution of the number of charged particles N_{ch} in the tracking system (FSD + GEM). The red marker corresponds to the distribution from the "outlier" RunId. Bottom panels: Mean multiplicity as a function of RunID. Black dotted horizontal line and red horizontal lines represent μ and $\pm 3\sigma$, respectively.

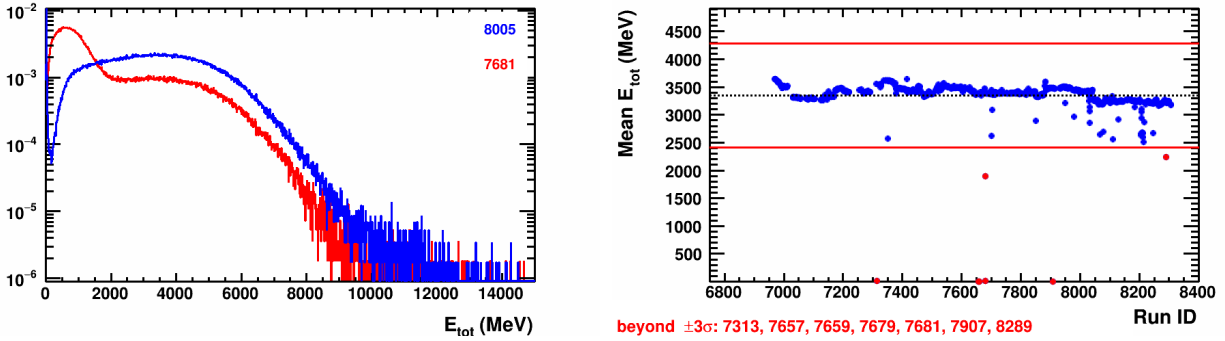


Figure 12: Left panel: distribution of the total energy E_{tot} of spectator fragments in the FHCAL. The red marker corresponds to the distribution from the "outlier" RunId. Right panel: Mean E_{tot} as a function of RunID. Black dotted horizontal line and red horizontal lines represent μ and $\pm 3\sigma$, respectively.

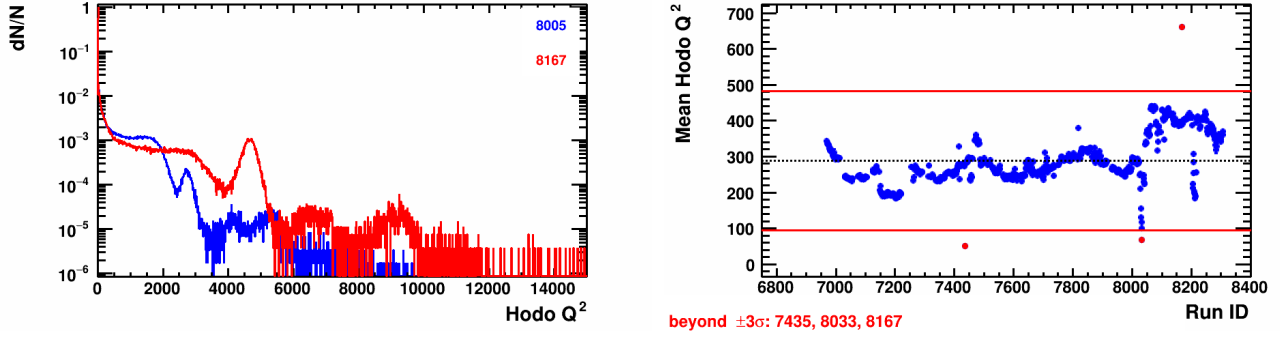


Figure 13: Left panel: distribution of the charge (Q^2) of spectator fragments in the forward quartz hodoscope (FQH). The red marker corresponds to the distribution from the "outlier" RunId. Right panel: Mean Q^2 as a function of RunID. Black dotted horizontal line and red horizontal lines represent μ and $\pm 3\sigma$, respectively.

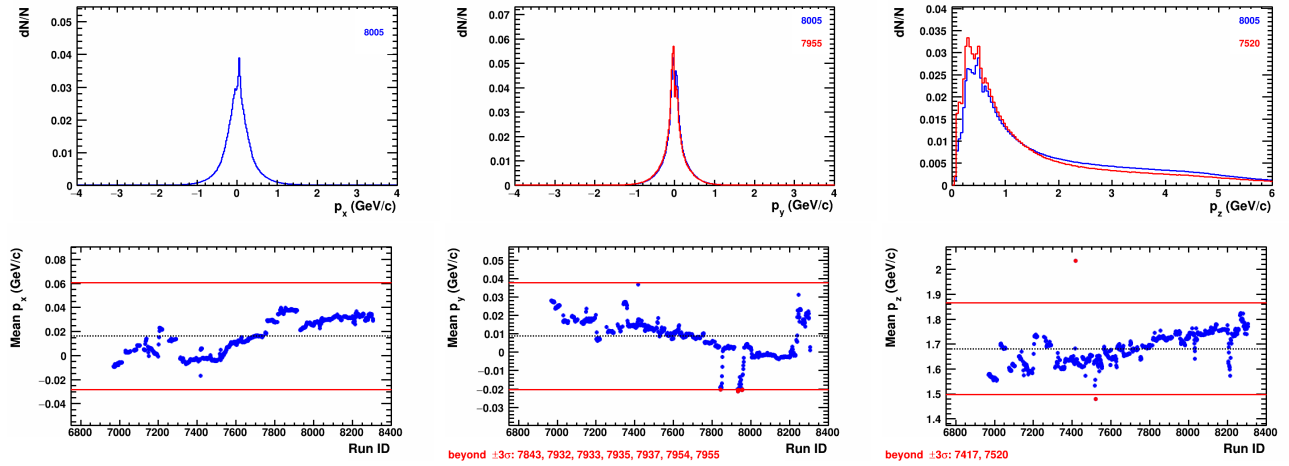


Figure 14: Upper panels: Distribution of the x, y and z components of momentum of charged particles. The red marker corresponds to the distribution from the "outlier" RunId. Bottom panels: Mean of x, y and z components of momentum as a function of RunID. Black dotted horizontal line and red horizontal lines represent μ and $\pm 3\sigma$, respectively.

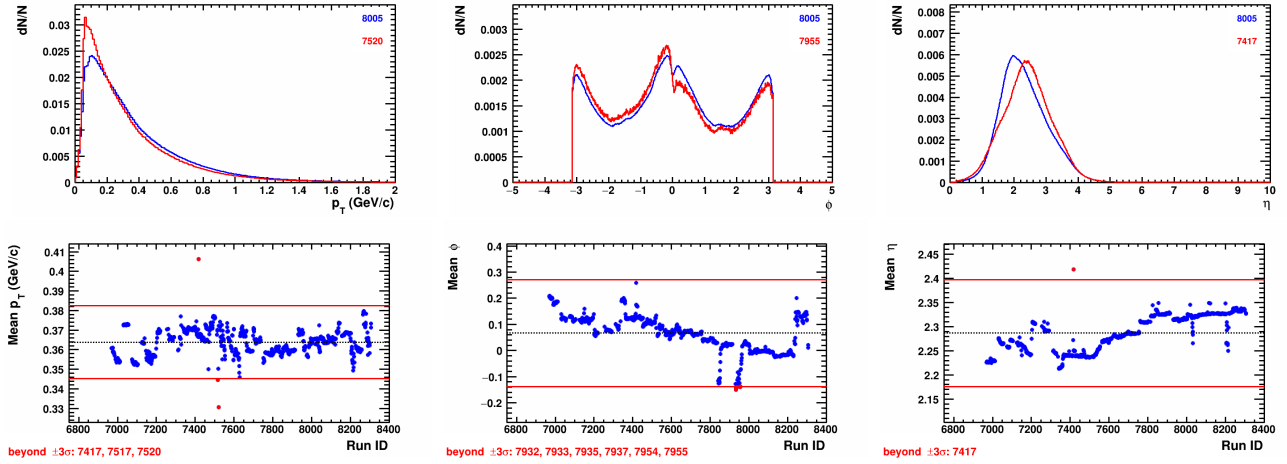


Figure 15: Upper panels: Distributions of the p_T (left), azimuthal angle ϕ (center) and η (right) of charged particles. The red marker corresponds to the distribution from the "outlier" RunId. Bottom panels: Mean p_T , ϕ and η as a function of RunID. Black dotted horizontal line and red horizontal lines represent μ and $\pm 3\sigma$, respectively.

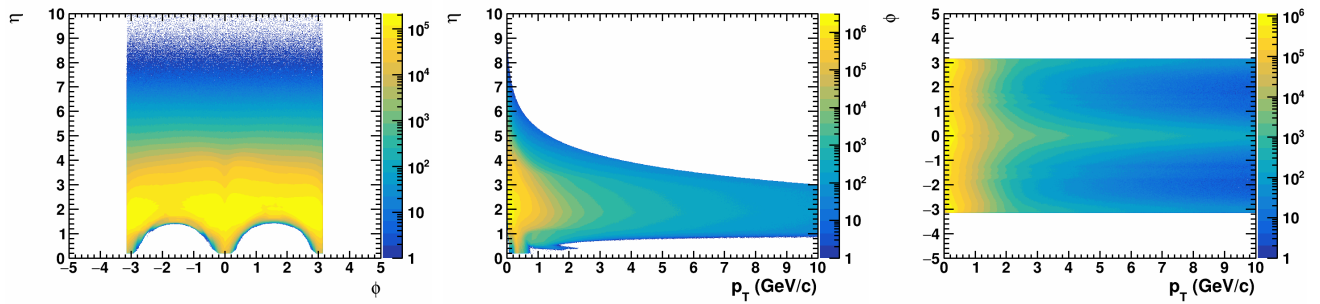


Figure 16: Correlation between the η and the ϕ (left), η and p_T (center), ϕ and p_T (right) for charged particles

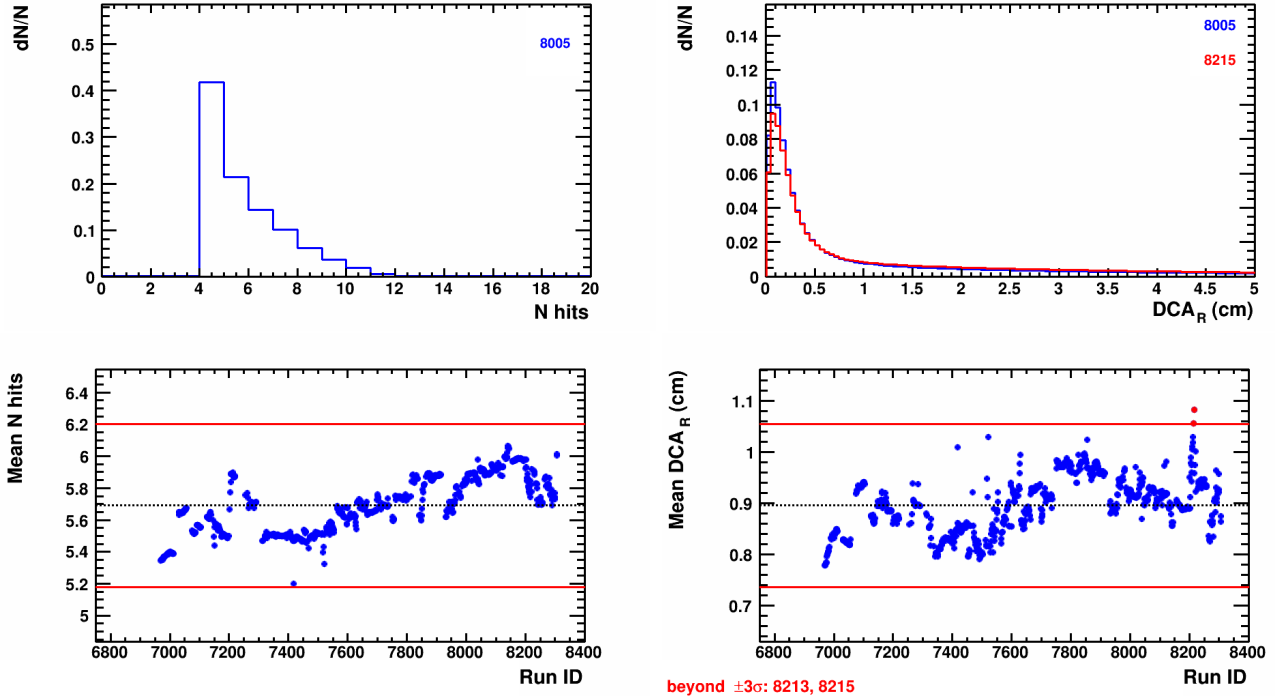


Figure 17: Upper panels: Distribution of the number of nHits to accurately reconstruct the track momentum (left) and the distance of closest approach DCA_R (right). The red marker corresponds to the distribution from the "outlier" RunID. Bottom panels: Mean nHits and DCA_R as a function of RunID. Black dotted horizontal line and red horizontal lines represent μ and $\pm 3\sigma$, respectively.

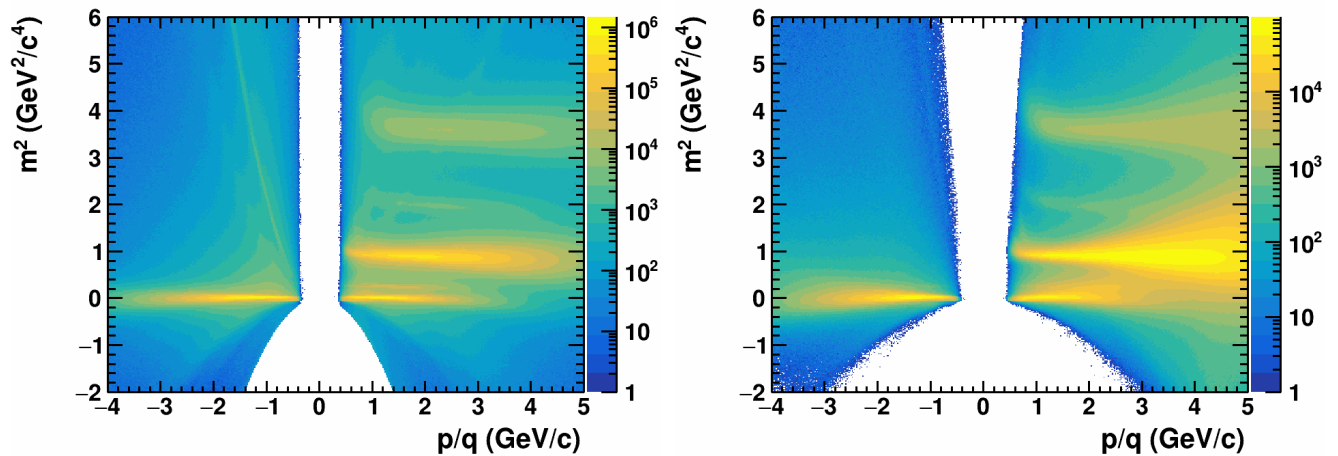


Figure 18: Population of charged particles in the mass squared (m^2) vs. laboratory momentum over charge (p/q) plane for the TOF-400 (left panel) and TOF-700 (right panel) detectors.

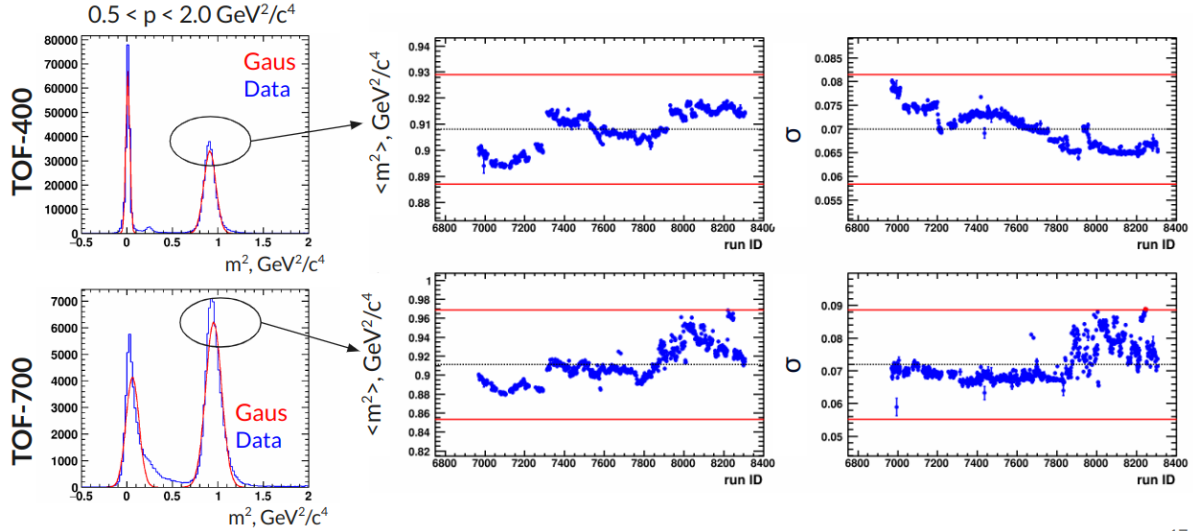


Figure 19: Distribution of the mass squared (m^2) and Gaussian fit of the proton peak in the TOF-400 (left upper panel) and TOF-700 (left bottom panel) detectors. Center and right panels: mean of the mass squared of proton and σ_{m^2} as a function of RunID. Black dotted horizontal line and red horizontal lines represent μ and $\pm 3\sigma$, respectively.

The preliminary list of bad runs based on QA study [18M events] RunId: 6968, 6970, 6972, 6973, 6975, 6976, 6977, 6978, 6979, 6980, 6981, 6982, 6983, 6984, 7313, 7326, 7415, 7417, 7435, 7517, 7520, 7537, 7538, 7542, 7543, 7545, 7546, 7547, 7573, 7575, 7657, 7659, 7679, 7681, 7843, 7847, 7848, 7850, 7851, 7852, 7853, 7855, 7856, 7857, 7858, 7859, 7865, 7868, 7869, 7907, 7932, 7933, 7935, 7937, 7954, 7955, 8018, 8031, 8032, 8033, 8115, 8121, 8167, 8201, 8204, 8205, 8208, 8209, 8210, 8211, 8212, 8213, 8215, 8289.

3.3 Data, Event and Track Selection

In total approximately 500 million events of Xe+Cs(I) collisions at the beam energy of 3.8A GeV were collected by the BM@N experiment in the January of 2023.

- 1) We don't consider runs below RunId=6924 due to unstable operation of the GEM and FSD detectors (BM@N Electronic Logbook).
- 2) We removed 74 runs [18M events] based on QA study, see section 3.2
- 3) We used events from Physical runs and CCT2 trigger [18].
- 4) at least 2 tracks in vertex reconstruction

5) The pileup events were rejected based on the $\pm 3\sigma$ cut on the correlation between the number of FSD digits and the number of charged particles in the tracking system (FSD + GEM), see the left and center panels of the Figure 20.

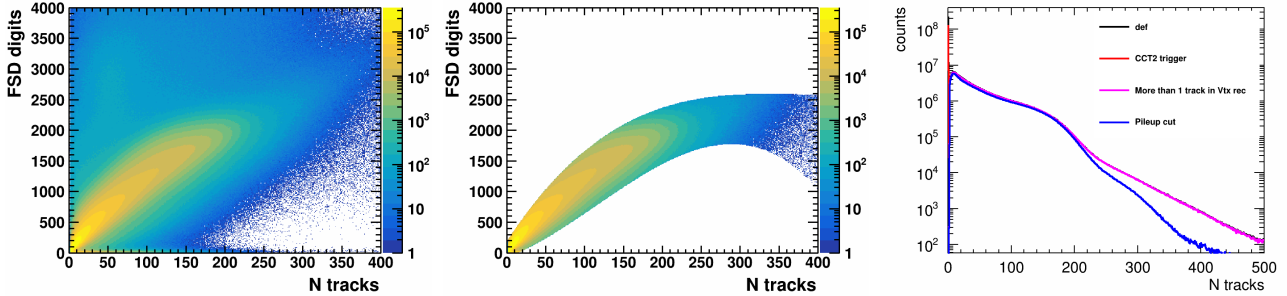


Figure 20: Left and center panels: Dependence of the number of FSD digits and the number of charged particles in the tracking system (FSD + GEM) before and after application of the pileup rejection cut. Right panel: tracks multiplicity distribution before and after applying the pileup rejection cut.

Table 1: Statistics after applying the selection criteria

Cuts	no. of events	%
def.	530 M	100%
CCT2 trigger	437 M	82%
at least 2 tracks in vertex reconstruction	315 M	59%
Pileup rejection cuts	285 M	53%
QA study	267 M	50%

Selection criteria are also imposed on tracks to ensure good tracks for analysis.

The selection cuts applied are as follows:

- 1) Tracks of charged particles were selected based on the number of stations N_{hits} in the BM@N inner tracking system used for track reconstruction. At least 6 were required to satisfy the criteria of a good track: $N_{hits} > 6$.
- 2) Only tracks with fit quality $\chi^2/NDF < 5$ were analyzed.
- 3) Distance of the closest approach (DCA) of tracks from the primary vertex in the direction perpendicular to the beam: $DCA < 5$ cm

Protons are identified using the time of flight Δt measured between T0 and the ToF

detectors, the length of the trajectory ΔL and the momentum p reconstructed in the BM@N central tracker. Then the squared mass m^2 of a particle is calculated. For each bin in momentum the position $\langle m_p^2 \rangle$ and the width $\sigma_{m_p^2}$ of the proton m^2 peak was extracted from the Gaussian fit. The procedure was done separately for TOF-400 and TOF-700 as they have different timing resolution. The proton samples selected by the requirements of $(m^2 - \langle m_p^2 \rangle) < 3\sigma_{m_p^2}$, see Figures 21–23.

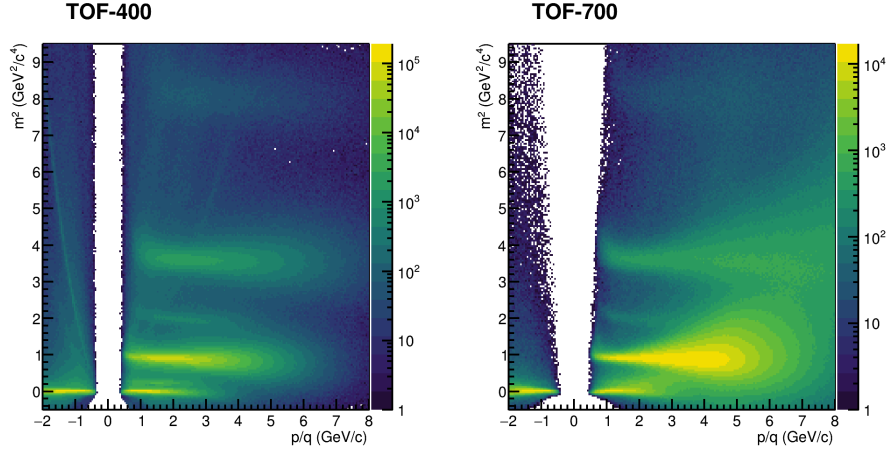


Figure 21: Population of charged particles in the m^2 vs. rigidity (p/q) plane for the TOF-400 (left panel) and TOF-700 (right panel) detectors.

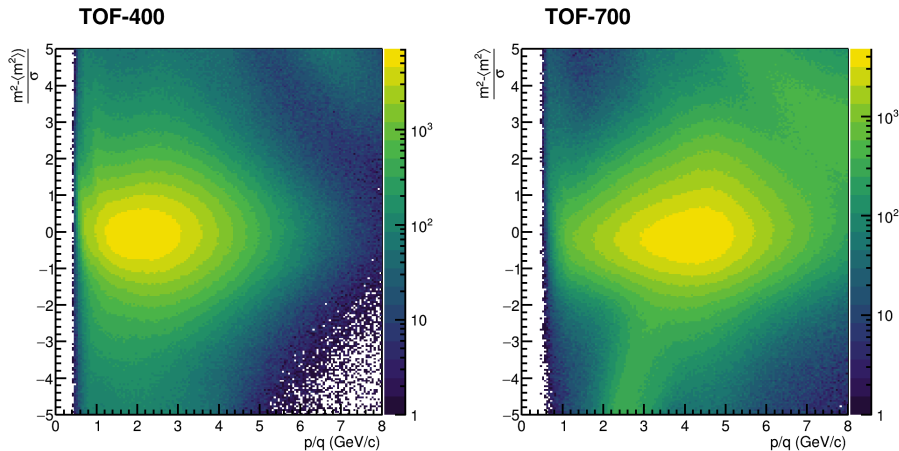


Figure 22: Population of charged particles in the $n\text{-}\sigma(m_p^2) = (m^2 - \langle m_p^2 \rangle) / \sigma_{m_p^2}$ vs. rigidity (p/q) plane for the TOF-400 (left) and TOF-700 (right) detectors.

Figure 24 shows the phase space coverage of identified protons as a function of rapidity y_{cm} and transverse momentum p_T for TOF-400, TOF-700 and for the

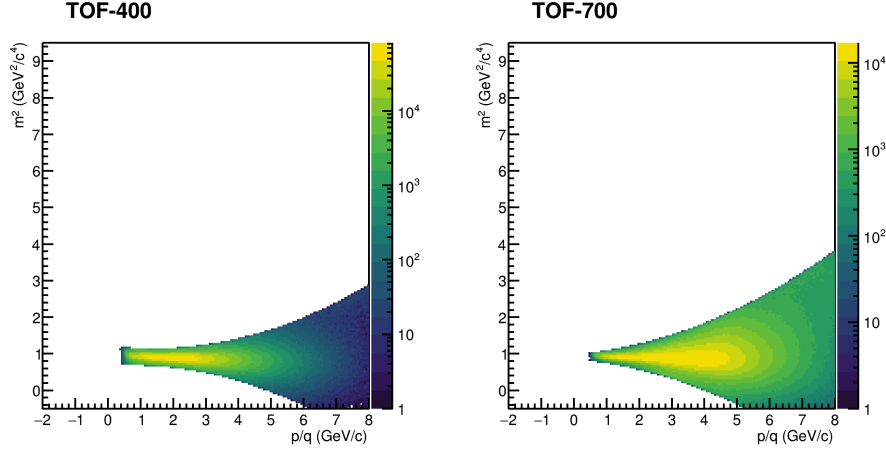


Figure 23: Population of selected protons in the m^2 vs. rigidity (p/q) plane for the TOF-400 (left) and TOF-700 (right) detectors. The protons were selected by $(m^2 - \langle m_p^2 \rangle) < 3\sigma_{m_p^2}$ cut.

combined system. Efficiency of the proton reconstruction was calculated using the realistic Monte-Carlo modelling of the BM@N experiment using GEANT4 transport code and JAM in the mean field mode events as an input. Efficiency of the proton reconstruction with the TOF-detectors acceptance applied is shown in the Figure. 25.

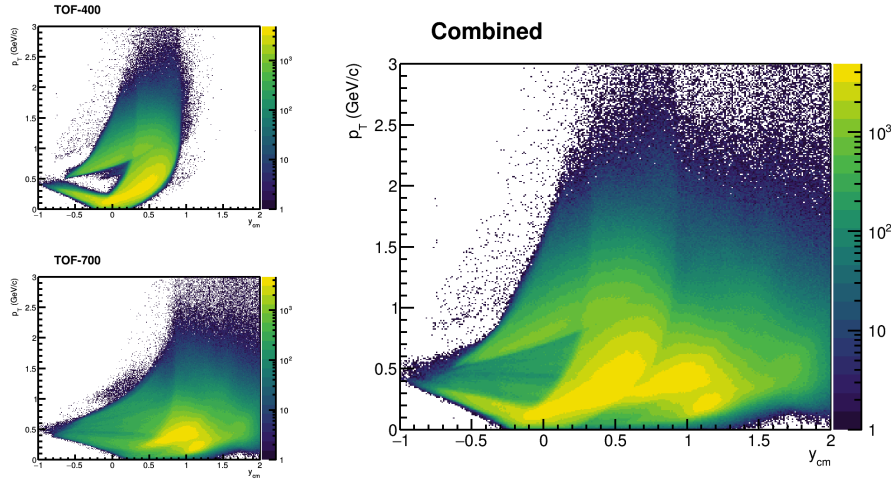


Figure 24: The phase space coverage of identified protons as a function of the centre-of-mass rapidity y_{cm} and transverse momentum p_T .

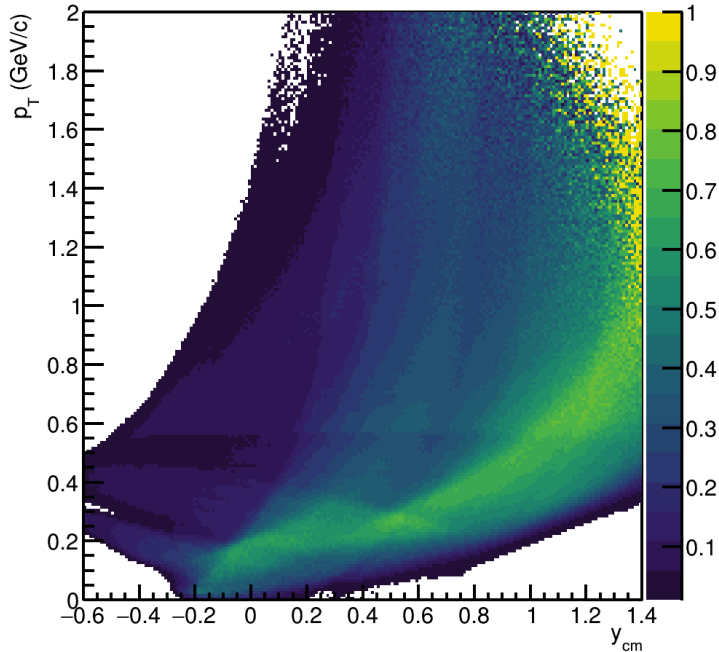


Figure 25: Efficiency of the proton reconstruction in the phase space of rapidity y_{cm} and transverse momentum p_T

3.4 Centrality determination

The size and evolution of the matter created in relativistic heavy-ion collisions strongly depend on collision geometry defined by the impact parameter. Since the impact parameter b of collisions (defined as the distance between the geometrical centers of the colliding nuclei in the transverse plane) cannot be accessed directly, the centrality classification can be based on the number of produced charged particle multiplicity N_{ch} in an event. Usually the correlation between the impact parameter b and the multiplicity N_{ch} is determined using the Monte-Carlo Glauber (MC-Glauber) method combined with a simple particle production model [29]. The modeled multiplicity is assumed to be a function of the number of participating nucleons (N_{part}) and the number of binary interactions between nucleons (N_{bin}), which one obtains from the output of the MC-Glauber model. The particle multiplicity distribution N_{ch}^{fit} can then be fitted to the experimentally measured one [30; 31]. Centrality classes are defined by sharp cuts on N_{ch} and corresponding mean values of $\langle b \rangle$ for each class determined from MC-Glauber events. While this approach offers a convenient parametrization of the measured N_{ch} distributions and the main classifier

for centrality determination in the STAR [11; 12] and HADES [32] experiments, it may suffer from large systematic uncertainties at low multiplicities and assumptions about the particle production mechanism [33]. In contrast to the MC-Glauber method, the recently proposed Γ -fit method does not require any modeling of the collision dynamics and can be used over a broad range of collision energies: from $\sqrt{s_{NN}}=5.44$ TeV [34] to the bombarding energy of 25 AMeV [35]. The Γ -fit method is based on the assumption that the relation between the measured N_{ch} and b is purely probabilistic and can be inferred from data without relying on any specific model of collisions. This typical inverse problem can be solved by a deconvolution method. A gamma distribution is used for the fluctuation kernel $P(N_{ch}|b)$ to model fluctuations of N_{ch} at a fixed impact parameter. The parameters of the gamma distribution were then extracted by fitting the measured distribution of N_{ch} [34; 35]. The application of both methods for centrality determination at NICA energies can be found in [17; 31; 36; 37].

In the first step, the validity of the procedures for centrality determination by the MC-Glauber and Γ -fit methods was assessed using the simulated data for Xe+Cs collisions at beam kinetic energy of 4 AGeV. The DCM-QGSM-SMM model [25] has been used to simulate around 2 M minimum bias Xe+Cs collision events. At the next step, the sample of events was made as an input for the full chain of realistic simulations of the BM@N detector subsystems based on the GEANT4 platform and reconstruction algorithms built in the BMNROOT framework for run8. The fully reconstructed events were used to generate the distributions of the multiplicity N_{ch} of the produced charged particles detected by FSD+GEM system, see left panel of Figure 26.

The 3.2 version of the PHOBOS MC-Glauber model [29] has been used to compose two nuclei out of nucleons and simulate their collision process event-by-event. An input of the MC-Glauber model is the nucleon density $\rho(r)$ inside the nucleus. It is usually parametrized by Fermi distribution:

$$\rho(r) = \rho_0 \frac{1 + w \left(\frac{r}{R}\right)^2}{1 + \exp \frac{r-R}{a}}, \quad (4)$$

where R is the radius of the nucleus, the constant ρ_0 corresponds to the density in the

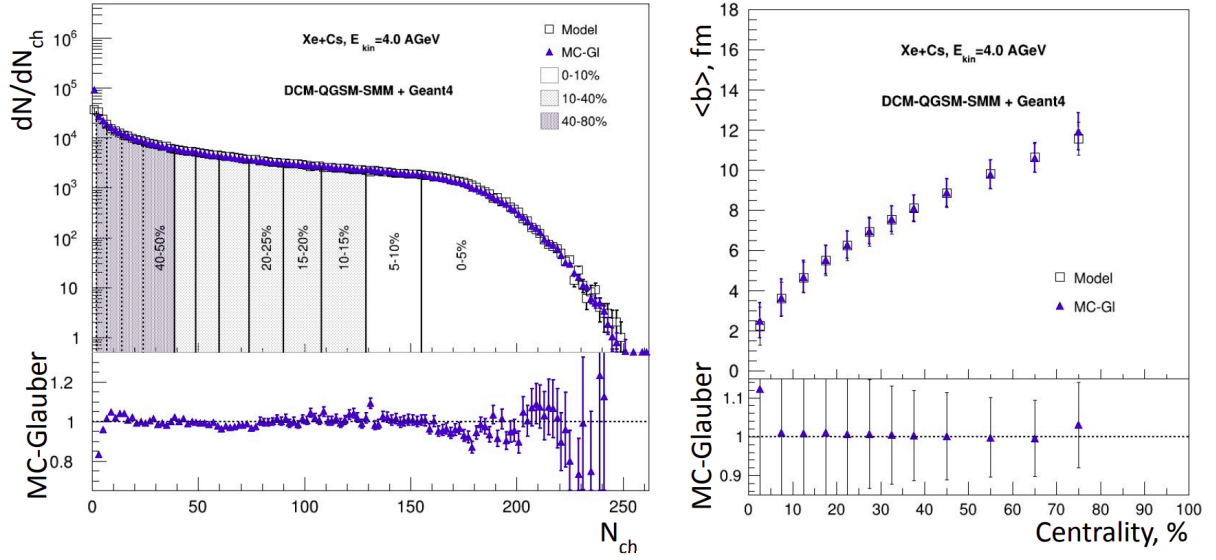


Figure 26: Left panel: FSD+GEM multiplicity distribution N_{ch} from the fully reconstructed DCM-QGSM-SMM model events (open squares) for Xe+Cs collisions compared to the fitted distribution using MC-Glauber approach (solid triangles). The centrality classes defined with MC-Glauber normalization are indicated with black vertical lines. Right panel: centrality dependence of the $\langle b \rangle$ from MC-Glauber approach (closed symbols) and directly from the model (open symbols) .

center of the nucleus. The skin thickness of the nucleus a defines how abruptly the density falls at the edge of the nucleus. The following parameters have been used: Xe ($A=129$, $Z=54$, $R=5.46$ fm, $a=0.57$ fm) and Cs ($A=133$, $Z=55$, $R=6.125$ fm, $a=0.5$). The nucleus-nucleus collision is treated as a sequence of independent binary nucleon-nucleon collisions, where the nucleons travel on straight-line trajectories and the inelastic nucleon-nucleon cross section σ_{NN}^{inel} assumed to depends only on the collision energy: $\sigma_{NN}^{inel}=27.7$ mb. Two nucleons from different nuclei are assumed to collide if the relative transverse distance d between centers is less than the distance corresponding to the inelastic nucleon-nucleon cross section: $d < \sqrt{\sigma_{NN}^{inel}/\pi}$. Geometrical properties of the collision, such as the impact parameter b , number of participating nucleons (N_{part}), and number of binary nucleon-nucleon collisions (N_{coll}), are calculated by simulating around 2 M minimum bias Xe+Cs collision events. The procedure for centrality determination includes fitting experimentally measured particle multiplicity N_{ch} with a MC-Glauber model based function $N_{ch}^{fit}(f, \mu, k)$ [30; 31;

36; 37] :

$$N_{ch}^{fit}(f, \mu, k) = N_a(f) \times P_{\mu,k}, \quad N_a(f) = fN_{part} + (1 - f)N_{coll}, \quad (5)$$

where $P_{\mu,k}$ is the negative binomial distribution (NBD) with mean μ and width k . $N_a(f)$ is a number of ancestors (number of independent sources), f characterizes the fraction of hard processes, N_{part} and N_{coll} are the number of participants and the number of binary collisions from MC-Glauber model output. The optimal set of parameters f , μ and k can be found from the minimization procedure is applied to find the minimal value of the χ^2 , which defined as follows:

$$\chi^2 = \sum_{i=n_{low}}^{n_{high}} \frac{(F_{fit}^i - F_{data}^i)^2}{(\Delta F_{fit}^i)^2 + (\Delta F_{data}^i)^2}, \quad (6)$$

where F_{fit}^i and F_{data}^i are values of the fit function and fitted histogram at a given bin i , ΔF_{fit}^i and ΔF_{data}^i are corresponding uncertainties, n_{low} and n_{high} are the lowest and highest fitting ranges correspondingly. A grid of k and f parameters was formed with corresponding χ^2 values for each (k, f) combination: $k \in [1, 50]$ with step of 1 and $f \in [0, 1]$ with step of 0.01. The framework and documentation for centrality determination by the MC-Glauber approach can be found in: <https://github.com/FlowNICA/CentralityFramework/tree/master/Framework/McGlauber>. As an example, left panel of Figure 26 shows by blue solid triangles the resulting N_{ch}^{fit} distribution from MC-Glauber fit. The ratio (N_{ch}^{fit}/N_{ch}) of the fit to the data shows the quality of the procedure, see the bottom part of Figure 26. After finding the optimal set of the fit parameters one can easily estimate the total cross-section and all events can be divided into groups with a given range of total cross-section (0-5%, 5-10% etc), see the black solid vertical lines in Figure 26. High multiplicity events have a low average b (central collisions) and low multiplicity events have a large average b (peripheral collisions). For each centrality class the mean value of the impact parameter $\langle b \rangle$ and its corresponding standard deviation was found using the information from the simulated MC-Glauber model events. Figure 26 (right panel) shows the

centrality dependence of $\langle b \rangle$ for the model events denoted by open symbols. The $\langle b \rangle$ from MC-Glauber approach (closed symbols) are presented for comparison.

In the Γ -fit method [34–37] the main ingredient is the fluctuation kernel which is used to model multiplicity fluctuations $P(N_{ch}|b)$ at a fixed impact parameter b . The fluctuations of the multiplicity can be described by the gamma distribution [34; 35]:

$$P(N_{ch}|b) = \frac{1}{\Gamma(k)\theta^k} N_{ch}^{k-1} e^{-N_{ch}/\theta} \quad (7)$$

where $\Gamma(k)$ is gamma function and two parameters $k(b)$ and $\theta(b)$ corresponding to the mean, $\langle N_{ch} \rangle$, and to the variance, $\sigma_{N_{ch}}$: $\langle N_{ch} \rangle = k\theta$, $\sigma_{N_{ch}} = \sqrt{k}\theta$. Similar to the multiplicity N_{ch} , which is always positive, the gamma distribution is only defined for $N_{ch} \geq 0$. It can be considered as a continuous version of the negative binomial distribution (NBD), which has long been used to fit multiplicity distributions in heavy-ion collisions [36; 37]. The normalized measured multiplicity distribution, $P(N_{ch})$, can be obtained by summing the contributions to multiplicity at all impact parameters:

$$P(N_{ch}) = \int_0^\infty P(N_{ch}|b)P(b)db = \int_0^1 P(N_{ch}|c_b)dc_b, \quad P(b) = \frac{2\pi b}{\sigma_{inel}} P_{inel}(b), \quad (8)$$

where $P(b)$ is the probability distribution of the impact parameter, and c_b denotes the centrality: $c_b \equiv \int_0^b P(b')db'$. $P(b)$ depends on the probability $P_{inel}(b)$ for an inelastic collision to occur at given b , and σ_{inel} is the inelastic nucleus-nucleus cross section. $P_{inel}(b) \simeq 1$ and $c_b \simeq \pi b^2/\sigma_{inel}$, except for peripheral collisions. For the variable k , one can use the following parameterization:

$$k(c_b) = k_0 \cdot \exp \left[- \sum_{i=1}^3 a_i (c_b)^i \right], \quad (9)$$

We fit $P(N_{ch})$ to the experimental distribution of N_{ch} using Eqs. (5) and (6) [34–37]. The fit parameters θ , k_0 and three coefficients a_i . The resulting parameters allow to reconstruct the probability of N_{ch} at fixed c_b : $P(N_{ch}|c_b)$. The fitting procedure

has been tested for the same charged particle multiplicity N_{ch} distribution, see left panel of Figure 27. The result of the Γ -fit is shown as red solid circles. The ratio plot shows that the Γ -fit method can reproduce the charged particle multiplicity distribution with a good accuracy.

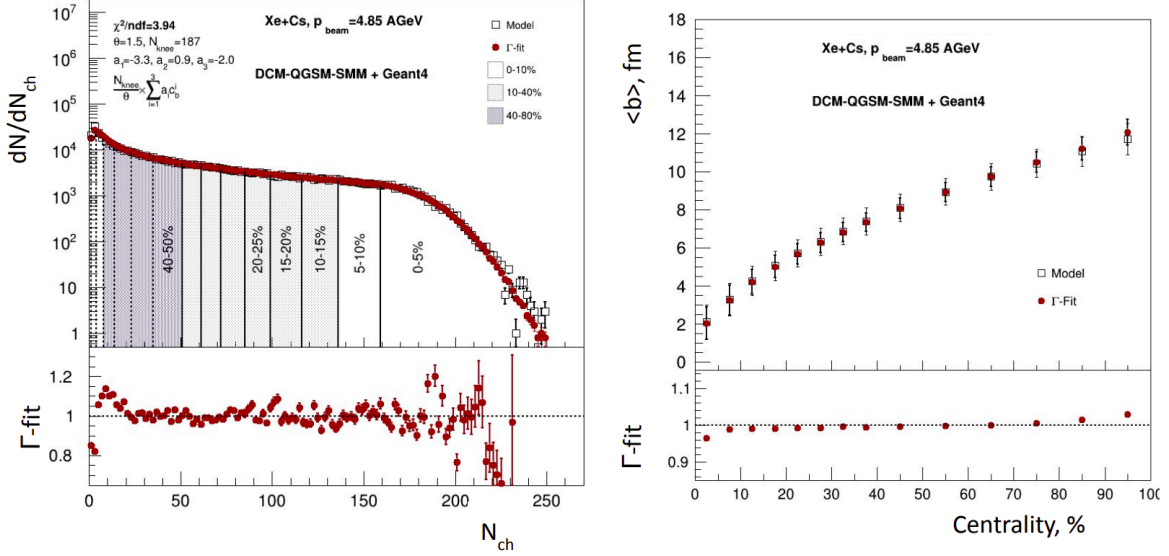


Figure 27: Left panel: FSD+GEM multiplicity distribution N_{ch} from the fully reconstructed DCM-QGSM-SMM model events (open squares) for Xe+Cs collisions compared to the fitted distribution using Γ -fit method (solid circles). The centrality classes defined with MC-Glauber normalization are indicated with black vertical lines. Right panel: centrality dependence of the $\langle b \rangle$ from Γ -fit method (closed symbols) and directly from the model (open symbols) .

Once the probability of N_{ch} at fixed c_b is reconstructed, the probability distribution of b , at fixed N_{ch} can be extracted by Bayes' theorem: $P(b|N_{ch}) = P(N_{ch}|b)P(b)/P(N_{ch})$, where $P(N_{ch}|b) = P(N_{ch}|c_b)$ and $c_b \simeq \pi b^2/\sigma_{inel}$ [34; 35]. Extending this reconstruction to a finite centrality bin, corresponding to an interval $N_{ch}^{low} < N_{ch} < N_{ch}^{high}$ is very straightforward upon integration over N_{ch} :

$$P(b|N_{ch}^{low} < N_{ch} < N_{ch}^{high}) = P(b) \frac{\int_{N_{ch}^{low}}^{N_{ch}^{high}} P(N'_{ch}|b) dN'_{ch}}{\int_{N_{ch}^{low}}^{N_{ch}^{high}} P(N'_{ch}) dN'_{ch}}, \quad (10)$$

where $\int_{N_{ch}^{low}}^{N_{ch}^{high}} P(N'_{ch}) dN'_{ch}$ is the width of the centrality bin Δc_b (i.e., 0.1 for the 0-10% centrality bin). 10% centrality classes defined with Γ -fit normalization are indicated with black solid vertical lines in Figure 27 (left). The framework and documentation for centrality determination by the Γ -fit method can be found in: <https://github.com/FlowNICA/CentralityFramework/tree/master/Framework/GammaFit>.

The centrality determination methods described above were applied to experimental BM@N data for Xe+Cs(I) collisions at 3.8 AGeV. To construct the multiplicity of charged particles (N_{ch}), we selected all events that satisfied the central collision trigger condition (CCT2), as well as events in which more than one track was used to reconstruct the collision vertex. The pile-up events were removed as well. Figure shows the results for determining centrality based on FSD+GEM multiplicity (open squares) using the MC-Glauber method (solid blue triangles) and the Γ -fit method (red solid circles). Both approaches describe the multiplicity distribution well up to 60%. The results of the Γ -fit method describe the experimental data in the mid-central region somewhat better. Figure 29 shows the resulting centrality dependence of the $\langle b \rangle$ from the MC-Glauber (blue solid triangles) and Γ -fit (red solid triangles). The results agree well for central collisions, but differ slightly for peripheral collisions. The results obtained provide a very preliminary estimate of collision centrality. To obtain the final results, it is necessary to evaluate the efficiency of the CCT2 trigger and take into account changes in the average FSD+GEM multiplicity during the run8, as well as to evaluate the systematics associated with the use of the MC-Glauber and Γ -Fit methods.

4 Methods for analyzing anisotropic flow in BM@N

4.1 General framework for the flow measurements

We start from the brief description of the general framework for the measurements of flow coefficients v_n in the fixed target experiment [2–5; 17]. The observables for v_n coefficients can be written in terms of flow Q_n and unit u_n vectors [4; 5; 17]. For each particle k in the event the unit $u_{n,k}$ vector in the transverse (x,y) plane can

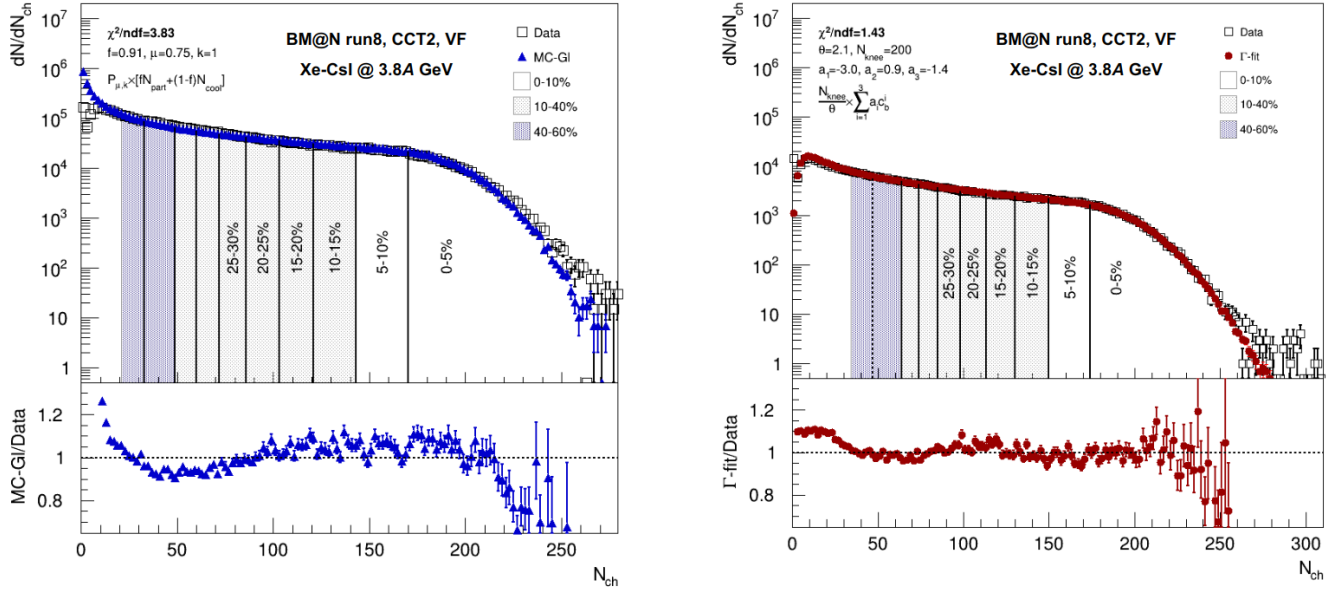


Figure 28: FSD+GEM multiplicity distribution N_{ch} from the BM@N run8 experimental data for Xe+Cs(I) collisions at 3.8 AGeV (open squares) compared to the fitted distribution using the MC-Glauber method (solid blue triangles) and Γ -fit method (red solid circles). The centrality classes are indicated with black vertical lines.

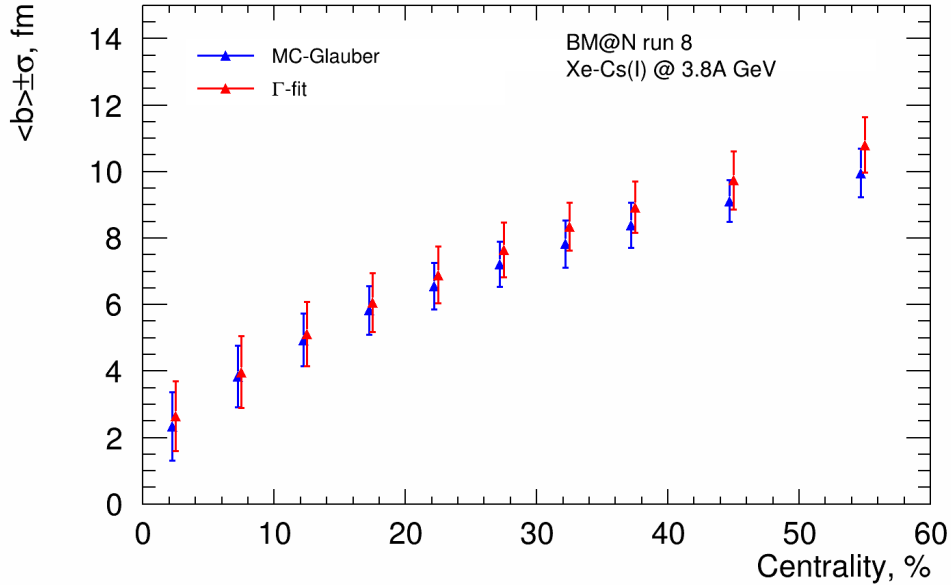


Figure 29: Centrality dependence of the $\langle b \rangle$ from the MC-Glauber (blue solid triangles) and Γ -fit (red solid triangles) methods for BM@N run8 experimental data: Xe+Cs(I) collisions at 3.8 AGeV.

be defined as:

$$u_{n,k} = e^{in\phi_k} = x_{n,k} + iy_{n,k} = \cos n\phi_k + i \sin n\phi_k, \quad (11)$$

where ϕ_k is the azimuthal angle of the particle's momentum. A two dimensional symmetry-plane (flow) Q_n -vector in the transverse plane is defined as a sum of unit $u_{n,k}$ -vectors over a group of particles in the event:

$$Q_n = \frac{\sum_{k=1}^M w_k u_{n,k}}{\sum_{k=1}^M w_k} = X_n + iY_n = |Q_n| e^{in\Psi_n^E}, \quad (12)$$

where M is the multiplicity of particles in the selected group, Ψ_n^E is the symmetry plane angle of n -th harmonic and w_k is the weight of particle, which is used either to correct the azimuthal anisotropy of the detector or to account for the multiplicity of particles falling into a specific cell of a segmented detector [4; 5; 17].

Detectors are not required to measure individual particles to be able to reconstruct the symmetry plane. As long as the detector is sensitive to the shape of the particle distribution in the transverse plane, the symmetry-plane (flow) Q_n vector can be determined. For the case of a segmented detector, such as a calorimeter, the mean position of the individual channels correspond to $u_{n,k}$. The channel amplitudes correspond to the weights w_k assigned to the $u_{n,k}$ in Eq. 12. A segmented detector needs a segmentation which is larger than $2n$ to be able to measure the Q_n vector of harmonic n .

At very large multiplicities in the selected group ($M \rightarrow \infty$) sum can be substituted by the integral and equation 12 can be transformed as follows:

$$\begin{aligned} \lim_{M \rightarrow \infty} Q_n &= \frac{\int_{2\pi} d\phi w(\phi) e^{in\phi} \rho(\phi - \Psi_n^R)}{\int_{2\pi} d\phi w(\phi) e^{in\phi} \rho(\phi - \Psi_n^R)} = \\ &= \frac{\int_{2\pi} d\phi w(\phi) e^{in\phi - \Psi_n^R} e^{in\Psi_n^R} \rho(\phi - \Psi_n^R)}{\int_{2\pi} d\phi w(\phi) e^{in\phi} \rho(\phi - \Psi_n^R)} = V_n e^{in\Psi_n^R}, \quad (13) \end{aligned}$$

where $V_n \propto v_n M$. From the equation above we can conclude that in limit of summation over very large group of particles in a event, $\Psi_n^E \rightarrow \Psi_n^R$ and Ψ_n^E is the estimation of reaction plane orientation in the event. We will refer to this estimation as sym-

metry plane of the collision or event plane of the collision.

Measurements of the azimuthal flow can be carried out projecting the u_n vector of selected particles onto symmetry plane of the collision (Scalar Product method):

$$v_n^{obs} = \frac{1}{2\pi} \langle u_n Q_n^* \rangle = \int d\Psi_n^R \int d\phi e^{in\phi} e^{-in\Psi_n^E} \rho(\phi - \Psi_n^R) = \langle \cos n(\phi - \Psi_n^R) V_n \cos n(\Psi_n^E - \Psi_n^R) \rangle. \quad (14)$$

Since the number of particles used for symmetry plane estimation is always limited, the cosine term with difference of symmetry plane angle and reaction plane angle will always be less than 1. Therefore correction R_n on the symmetry plane resolution is needed. This correction is provided using the resolution correction coefficient R_n defined as follows:

$$R_n = \langle V_n \cos n(\Psi_n^E - \Psi_n^R) \rangle. \quad (15)$$

Then the unbiased observable for the azimuthal flow of particles is defined by following equation:

$$v_n = \frac{v_n^{obs}}{R_n} = \frac{\langle u_n Q_n^* \rangle}{R_n}. \quad (16)$$

Since the reaction plane of the collision is unknown, calculation of the resolution correction factor R_n can be performed using the pairwise correlations of Q_n vectors:

$$\langle Q_n^a Q_n^{b*} \rangle = \langle V_n^a \cos n(\Psi_n^a - \Psi_R) V_n^b \cos n(\Psi_n^b - \Psi_R) \rangle, \quad (17)$$

where a and b indices indicate two groups of particles in each of which the symmetry plane $\Psi_n^{a,b}$ estimation was carried out separately. In this work the resolution correction factor was calculated using the method of three sub-events. Using three groups of particles, say a , b and c , we can estimate resolution via this formula:

$$R_n\{a(b, c)\} = \sqrt{\frac{\langle Q_n^a Q_n^b \rangle \langle Q_n^a Q_n^c \rangle}{\langle Q_n^b Q_n^c \rangle}} \quad (18)$$

To suppress the correlations not correspondent to the initial collective motion of the produced particles (non-flow) we suggest defining a group of particles with sufficient (pseudo-) rapidity separation between each of symmetry planes a , b and c . In the case where this separation cannot be achieved (for example a and b or a and c are not separated) we can introduce additional symmetry plane vector d , and require (pseudo-) rapidity separation only between three of the event planes, say a and d , b and d , c and d and c and d . Slight modification of the three sub-event method produces the estimation of resolution correction factor produces which we going to call the method of four sub-events:

$$R_n\{a(d)(b, c)\} = \langle Q_n^a Q_n^d \rangle \sqrt{\frac{\langle Q_n^d Q_n^b \rangle \langle Q_n^d Q_n^c \rangle}{\langle Q_n^b Q_n^c \rangle}} \quad (19)$$

In this work we use the symmetry plane defined from the spectator energy deposition in a modular detector FHCAL. In this case the first-order symmetry plane Q_1 can be estimated using the modification of formula 12:

$$Q_1 = \sum_{k=1}^N E_k e^{i\varphi_k} / \sum_{k=1}^N E_k, \quad (20)$$

where φ is the azimuthal angle of the k -th FHCAL module, E_k is the signal amplitude seen by the k -th FHCAL module, which is proportional to the energy of spectator. N denotes the number of modules in the group. To suppress the auto-correlations between u_n and Q_n vectors we rejected protons with projected position in FHCAL plane within the acceptance of FHCAL.

Since the reaction plane orientation is random and uniform, in the case of the ideal detector acceptance, correlation of vectors can be substituted with the correlation of their components (for more details see [3; 4; 17]):

$$\langle Q_n^a Q_n^b \rangle = 2\langle X_n^a X_n^b \rangle = 2\langle Y_n^a Y_n^b \rangle, \quad (21)$$

or similarly for the three-particles correlation:

$$\langle Q_{2n}^a Q_n^b Q_n^c \rangle = 4 \langle X_{2n}^a X_n^b X_n^c \rangle = 4 \langle X_{2n}^a Y_n^b Y_n^c \rangle = 4 \langle Y_{2n}^a X_n^b Y_n^c \rangle = -4 \langle Y_{2n}^a Y_n^b X_n^c \rangle. \quad (22)$$

Based on this, one can use only correlations of components of Q_n and u_n vectors to calculate flow coefficients.

$$v_n = 2 \frac{\langle x_n X_n^* \rangle}{R_n^x} = 2 \frac{\langle y_n Y_n^* \rangle}{R_n^y}, \quad (23)$$

where $R_n^{x,y}$ notate values of resolution correction coefficient calculated using the X and Y components of Q_n -vectors.

For instance, equation 23 for v_1 can be rewritten as follows:

$$v_1 = \frac{2 \langle y_1 Y_1^a \rangle}{R_1^y \{a\}}, \quad (24)$$

where y_1 and Y_1^a are y -components of u_1 and Q_1^a vectors respectively, and $R_1^y \{a\}$ is the resolution correction factor for Y_1^a :

$$R_1^y \{a(b, c)\} = \sqrt{\frac{2 \langle Y_1^b Y_1^c \rangle}{2 \langle Y_1^a Y_1^b \rangle 2 \langle Y_1^a Y_1^c \rangle}}, \quad (25)$$

In case of an ideal detector, the Q_n -vector relation to the symmetry plane is limited only by the multiplicity of the particles within the acceptance. In reality, the detector non-uniformity in ϕ and effects from the magnetic field, additional material etc., can bias the flow measurements. This leads to equations 21 and 22 are being no longer valid. Detector non-uniformities can be treated on the level of the flow Q_n vectors. The following procedure was introduced in [4]. The advantages compared to re-weighting of the azimuthal particle spectra is that the procedure also works with detectors that have holes in the azimuthal acceptance. The necessary correction factors can be fully determined from the data itself. Monte Carlo simulations are not needed. The corrections (re-centering, twist and rescaling) can also be generalized to a generic normalized flow vector q_n with the components x_n and y_n . Schematic

representation of these corrections are shown in Figure 30.

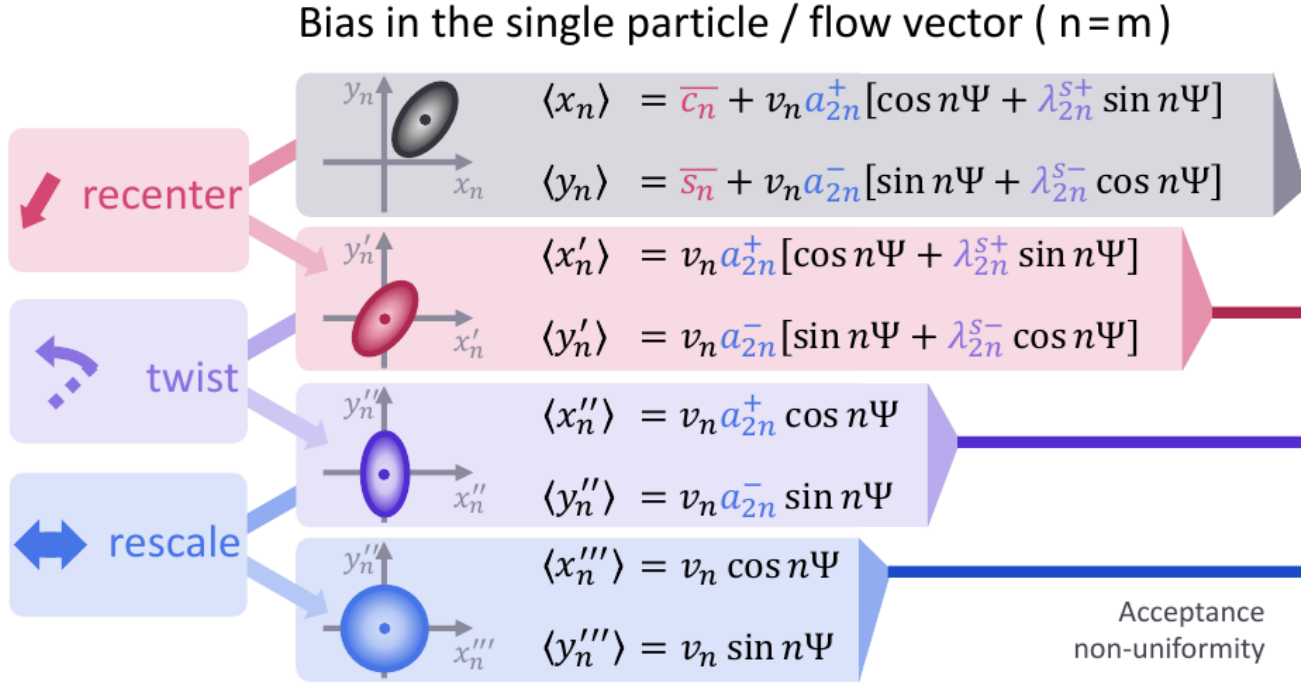


Figure 30: Schematic illustration of recentering, twist and rescale correction steps for q_n -vector introduced in [4].

Re-centering: A static shift of the detector signals can manifest in a shift of the average flow vector away from the origin. This shift can be removed by subtracting the mean flow vector from the flow vector in each collision.

Twist/Diagonalization: The flow vector distribution can appear twisted, if $\sin(n\Psi)$, or $\cos(n\Psi)$ terms bias the x_n and y_n components of the flow vectors. The diagonalization corrections are calculated from the averaged flow vector components and applied to the flow vector in each collision.

Rescaling: A squashed flow vector distribution, which corresponds to different widths in the x and y direction, can be corrected with the rescaling correction.

The formalism of these corrections has been implemented in a software framework known as QnTools[38], which allows to perform the corrections of differential flow vectors, which may depend on a number of particle properties $q_n(p_T, \eta, PID, \dots)$, see Figure 31.

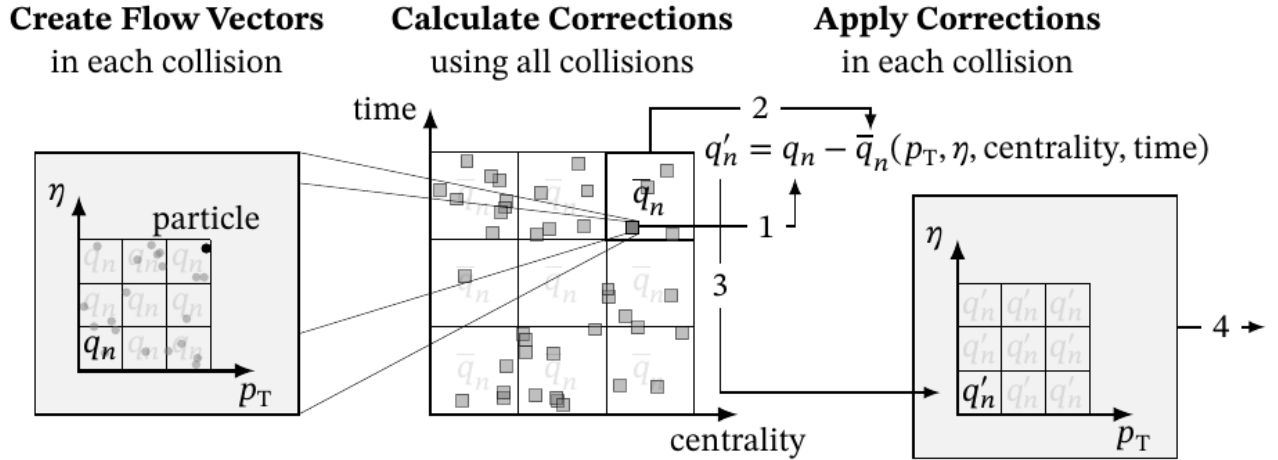


Figure 31: Sketch of the multi-dimensional correction procedure in the QnTools framework. As an example the recentering correction as a function of p_T , η , centrality, and time is shown.

4.2 BM@N performance for flow measurements

In this subsection, we discuss the anticipated performance of BM@N experiment [18] in the configuration for run8 for differential anisotropic flow measurements of identified hadrons at Nuclotron energies $\sqrt{s_{NN}} = 2.3\text{-}3.5$ GeV, see [17] for the details. As the main event generator we have used the JAM (RQMD.RMF) model [26–28] with momentum dependent mean field [28], which qualitatively describes the existing measurements of directed and elliptic flow of protons at this energy range [17; 21]. We generated about 5 M minimum bias Xe+Cs(I) collision events for each beam energy: 2, 3 and 4 AGeV. At the next step, the sample of JAM model events was made as an input for the full chain of realistic simulations of the BM@N detector subsystems for run8 based on the GEANT4 platform and reconstruction algorithms built in the BMNROOT framework. The fully reconstructed events were used to generate the distributions of the multiplicity N_{ch} of the produced charged particles detected by FSD+GEM system of the BM@N [18] and estimate the centrality, see the section 3.4 for the details.

The tracking system allows to reconstruct the momentum p of the particle with a momentum resolution of $\Delta p/p \sim 1.7\text{-}2.5\%$ for the kinetic energy 4A GeV (magnetic field 0.8 T). For the experiment at lower kinetic energy 2 AGeV one needs to use the reduced magnetic field 0.4 T. This leads to a deterioration in the momentum

resolution, see the left part of the Figure 32. Charged-hadron identification is based on the time-of-flight measured with TOF-400 and TOF-700. The time resolutions of the ToF-400 and ToF-700 systems are 80 ps and 115 ps, respectively. Particle velocity is obtained from the measured flight time and flight path. Combining this information with the particle momenta p allows to identify charged hadrons with high significance. As an example, the right part of the Figure 32 shows the population of all charged particles in the plane spanned by their β and momenta divided by charge (rigidity) for the TOF-400.

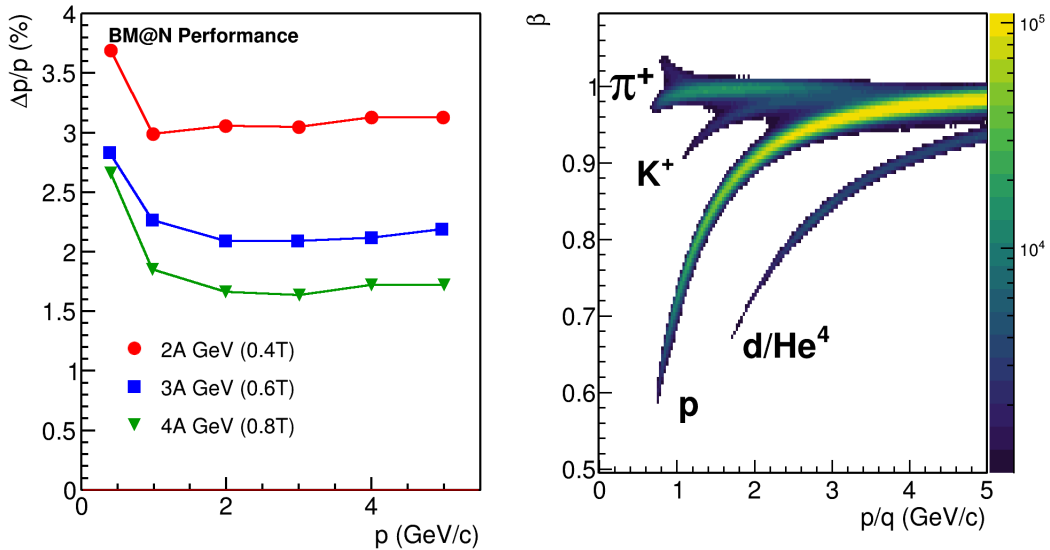


Figure 32: Left: Relative momentum resolution $\Delta p/p$ as a function of the momentum p for fully reconstructed charged tracks from Xe+Cs(I) collisions generated using the JAM model at different kinetic energies: 4 AGeV (triangles), 3 AGeV (boxes) and 2 AGeV (circles). Right: Population of the reconstructed charged particles in the velocity β vs. laboratory momentum over charge (p/q) plane for the TOF-400.

Symmetry plane estimation was carried out in assumption that spectator fragments are pushed in reaction plane by the expanding overlap region of colliding nuclei and they have positive directed flow signal $v_1 > 0$ in the forward rapidity region [3; 4]. The Forward Hadron Calorimeter (FHCAL) registers the energy deposition of spectator fragments in the BM@N experiment. Modules of the FHCAL were divided into three groups according to the ranges of pseudorapidity in the laboratory frame η : (F1) $4.4 < \eta < 5.5$; (F2) $3.9 < \eta < 4.4$; and (F3) $3.1 < \eta < 3.9$, see the left part of Figure 38. The Q_1 vectors for each sub-event (F1, F2, F3) in the FHCAL have

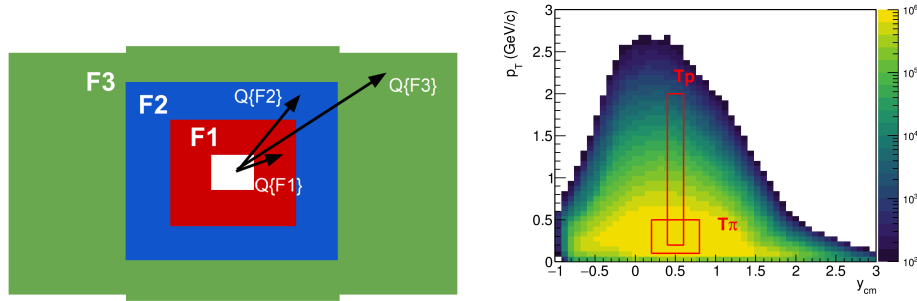


Figure 33: Left part: schematic representation of modules of the Forwar Hadron Calorimeter divided in 3 groups. The corresponding sub-events are represented with different colors. Arrows denote the Q_1 -vectors for each sub-event in FHCaL (F1,F2,F3). Right part: schematic representation of kinematic windows for Q_1 -vectors from tracks (Tp and $T\pi$), see text for the details.

been obtained as follows:

$$Q_1 = \sum_{k=1}^N E_k e^{i\varphi_k} / \sum_{k=1}^N E_k, \quad (26)$$

where φ is the azimuthal angle of the k -th FHCaL module, E_k is the signal amplitude seen by the k -th FHCaL module, which is proportional to the energy of spectator. N denotes the total number of modules in the given sub-event. Two additional sub-events were introduced from the tracks of the charged particles in the inner tracking system of BM@N. For the first group we used the protons (Tp) in the kinematic window of $0.4 < y_{cm} < 0.6$ and $0.2 < p_T < 2.0 \text{ GeV}/c$ and the negative charged pions ($T\pi$) for the second group with $0.2 < y_{cm} < 0.8$ and $0.1 < p_T < 0.5 \text{ GeV}/c$. The Q_1 vectors defined from the tracks of charged particles (Tp and $T\pi$) are calculated according to Eq. 12, see the right panel of Figure 38.

The left part of Figure 34 shows the acceptance for selected protons: azimuthal angle φ vs center-of-mass rapidity y_{cm} . The azimuthal coverage of the tracking system in the BM@N is strongly non-uniform. QnTools framework [38] with recentering, twist and rescaling corrections has been applied for both u_1 and Q_1 vectors. The right part of Figure 34 shows the y_{cm} dependence of v_1 of protons with $0.2 < p_T < 0.6 \text{ GeV}/c$ from 10-30% central Xe+Cs(I) collisions. The black solid line denotes the v_1 values of protons directly from the JAM model. The symbols denote the

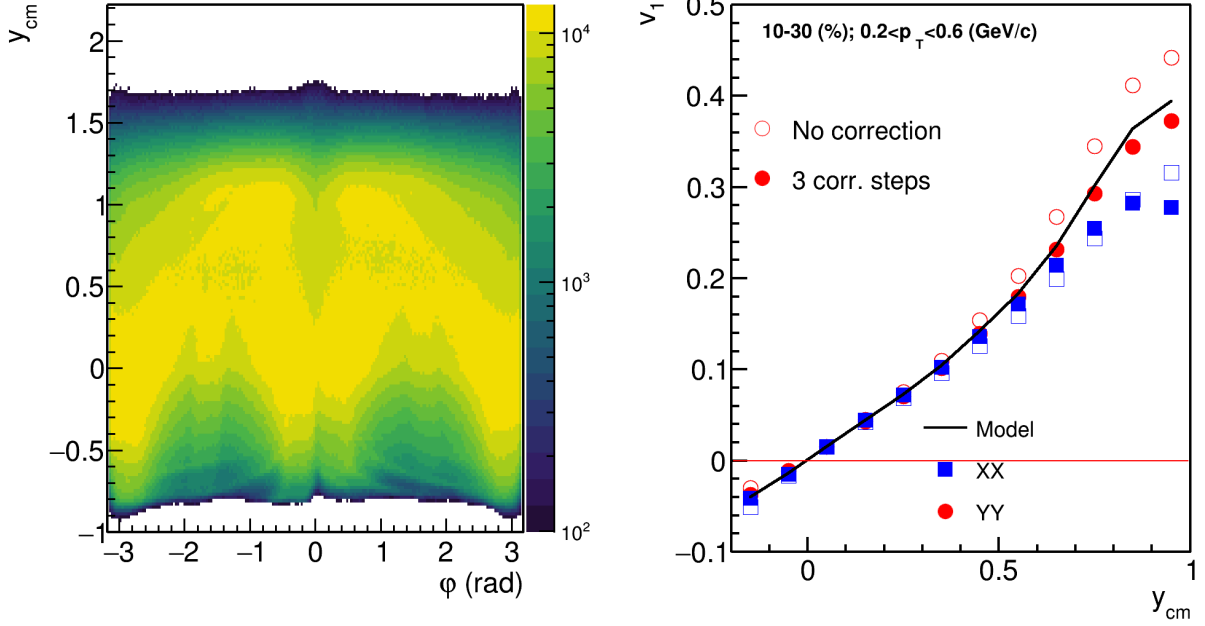


Figure 34: (Left) Raw yield of protons as a function of azimuthal angle φ and center-of-mass rapidity y_{cm} . (Right) Comparison of the directed flow v_1 signal of protons before (open symbols) and after (closed symbols) corrections on the non-uniformity of azimuthal acceptance, see the text for the details.

$v_1(y_{cm})$ values of protons from the analysis of the fully reconstructed model events: before (open symbols) and after corrections for the non-uniform azimuthal acceptance (closed symbols). The application of corrections yields to a better agreement between the reconstructed (closed symbols) and the model (line) v_1 signals in the full range of rapidity. The agreement between reconstructed and model values of v_1 is better for the results obtained using the YY correlation of vectors. The magnetic field of BM@N is directed along the y axis and it deflects the produced charged particles in x direction. This may introduce the additional correlation between the XX components of the vectors and increase the difference between the reconstructed v_1 calculated from the correlation of XX components and the v_1 values from the JAM model.

Figure 35 shows the centrality dependence of resolution correction factor R_1 for the different combinations of Q_1 -vectors in the 3 and 4-subevents methods for F1, F2 and F3 symmetry planes from left to right. Due to the propagation of hadronic shower between the FHCAL modules in the transverse direction, the estimations for

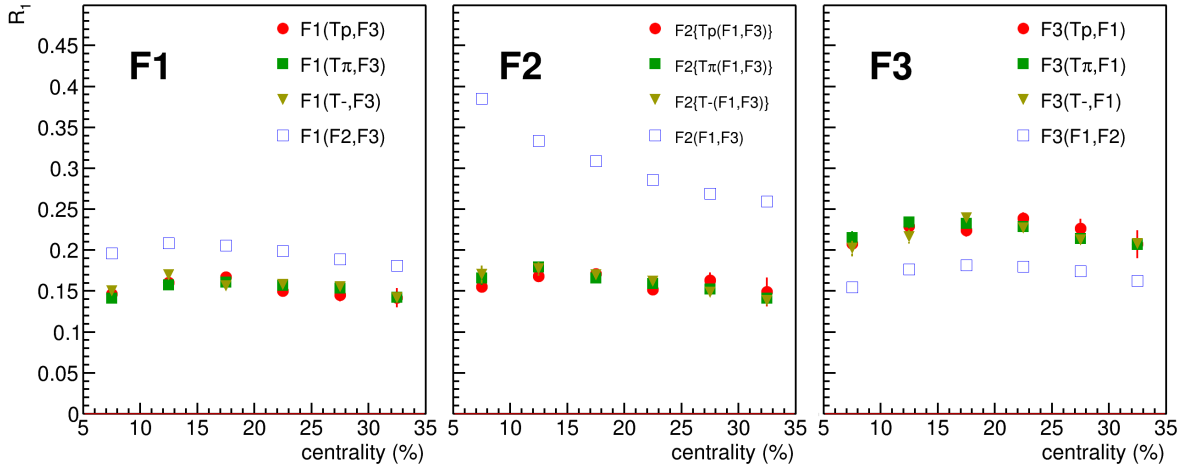


Figure 35: The centrality dependence of resolution correction factor R_1 for different combinations of Q_1 -vectors in the 3 and 4-subevents methods for F1, F2 and F3 symmetry planes from left to right.

the R_1 resolution factor for the combinations of neighboring sub-events such as F1 and F2 or F2 and F3 will be strongly biased (blue markers). In contrast, the R_1 values calculated using the combinations with significant rapidity separation (red, green and yellow markers) are found to be in agreement within the statistical errors. Figure 36 shows the centrality dependence of the resolution correction factor for the spectator symmetry plane for different beam energies: 2 AGeV (left), 3 AGeV (middle) and 4 AGeV (right). For all symmetry planes F1, F2, F3 we observe a decrease of the resolution correction factor R_1 with increasing energy. Shortening of the passage time of colliding nuclei at higher energies leaves less time for the interaction between the matter produced within the overlap region and spectators, which leads to the smaller values of the spectators directed flow and smaller magnitude of Q_1 -vectors. As a consequence, one can expect smaller values for the resolution correction factor R_1 .

Figure 37 shows the directed v_1 (left part) and elliptic v_2 flow (right part) signals of protons from the analysis of JAM model events for 10-30% central Xe+Cs(I) collisions at 2 AGeV (circles), 3 AGeV (boxes) and 4 AGeV (triangles). Markers represent the v_n results from the analysis of the fully reconstructed JAM model events and lines the results obtained directly from the model (output model particles without reconstruction were correlated with the RP). A good agreement is

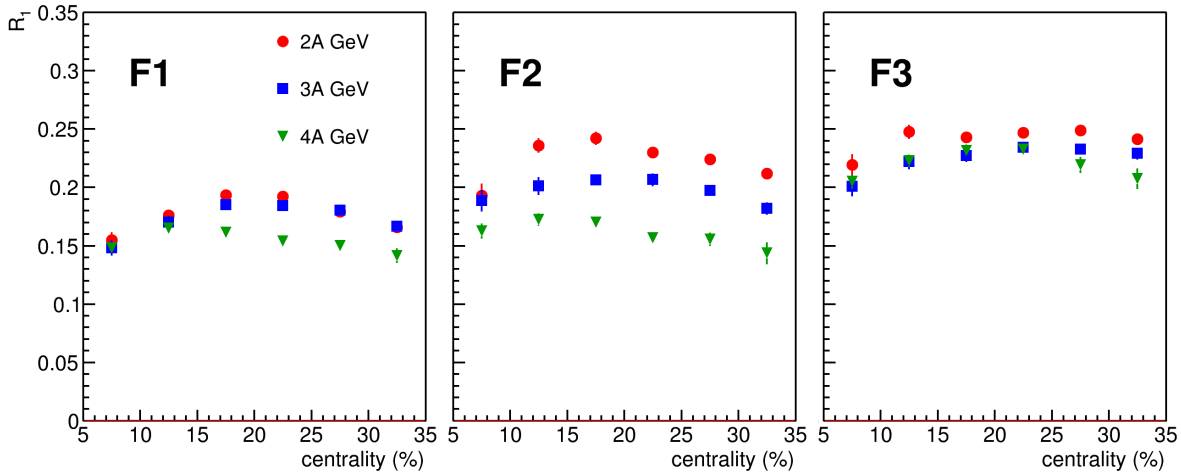


Figure 36: The centrality dependence of the resolution correction factor R_1 for spectator plane. The results are presented for sub-events F1, F2 and F3: panels from left to right. Different symbols correspond to the results for Xe+Cs(I) collisions at different beam energies: 2, 3 and 4A GeV.

observed between these two sets of v_n results.

4.3 The analysis of v_1 of protons from BM@N run8 data

In this subsection, we discuss the details of analysis of directed flow v_1 of protons in Xe+Cs(I) collisions at 3.8 AGeV using the BM@N run8 data.

- 1) To address the effects of the non-uniform acceptance we applied the corrections for both u_1 and Q_1 vectors :recentering, twist and rescaling. The QnTools framework [38] was used for corrections of u_1 and Q_1 vectors and flow analysis. For u_1 -vector corrections were employed multi-differentially on transverse p_T , rapidity y and centrality. For the Q_1 -vectors corrections were applied only differentially on centrality.
- 2) The detailed performance study, persented in the previus subsection, shows that due to magnetic field acting along the y -axis and deflecting charged particles along the x axis, we can measure the directed flow v_1 of protons using only the y components of flow vectors:

$$v_1 = 2 \frac{\langle y_1 Y_1^{a*} \rangle}{R_1^y \{a\}}, \quad (27)$$

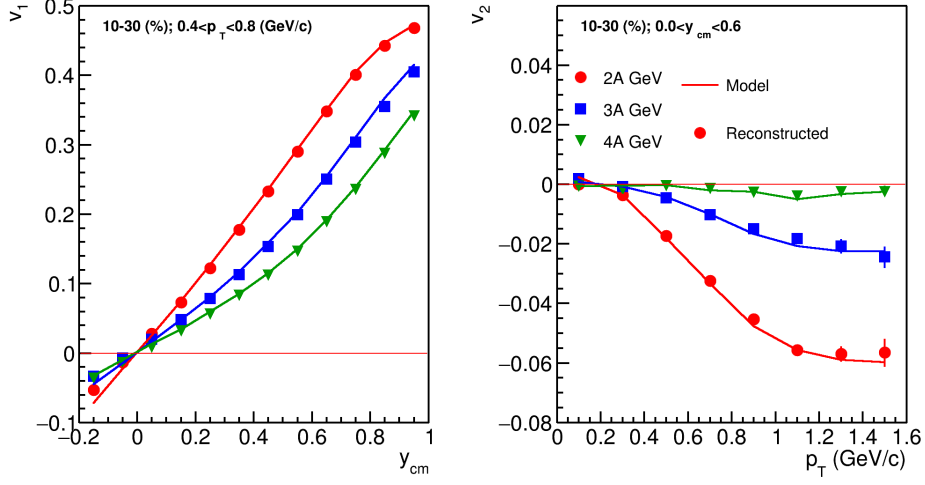


Figure 37: Left: directed flow v_1 of protons as a function of center-of-mass rapidity y_{cm} for 10-30% central Xe+Cs(I) collisions at 2 AGeV (circles), 3 AGeV (boxes) and 4 AGeV (triangles); Right: elliptic flow v_2 of protons as a function of transverse momentum p_T . Markers represent the results of the analysis of the fully reconstructed JAM model data and lines the results obtained directly from the model. Figure is taken from [17]

where the resolution correction factor is calculated using the method of three sub-events:

$$R_1^y\{a(b, c)\} = \sqrt{\frac{\langle Y_1^a Y_1^b \rangle \langle Y_1^a Y_1^c \rangle}{\langle Y_1^b Y_1^c \rangle}}, \quad (28)$$

or by the four sub-event method:

$$R_1^y\{a(d)(b, c)\} = \langle Y_1^a Y_1^d \rangle \sqrt{\frac{\langle Y_1^d Y_1^b \rangle \langle Y_1^d Y_1^c \rangle}{\langle Y_1^b Y_1^c \rangle}}, \quad (29)$$

3) The Q_1 vectors for symmetry planes in the FHCAL have been obtained using the Eq. 26. Modules of the FHCAL were divided into three groups (sub-events): F1, F2, F3 as it is shown in the Figure. 38. According to the simulations, due to charge splitting in the dipole analyzing magnet SP-41, F1 sub-event primarily registers the spectator protons, F2 — spectator fragments and F3 — neutrons, see the left part of Figure. 38.

Two additional sub-events were introduced from the tracks of the charged particles in the inner tracking system of BM@N. All negatively charged particles with

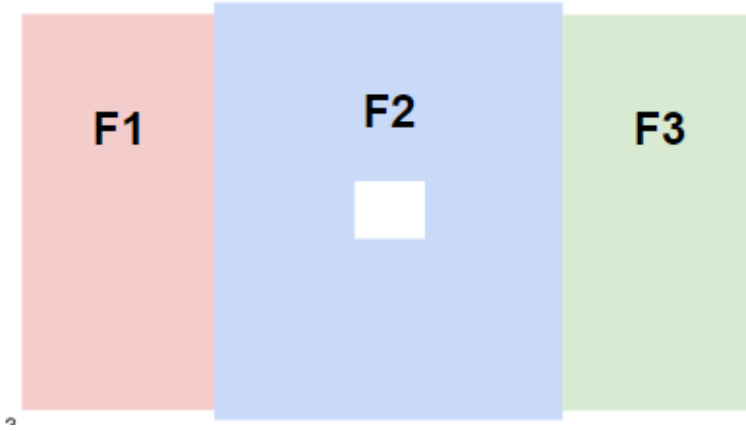


Figure 38: Layout of the FHCAL modules division into three groups (sub-events): F1, F2, F3.

pseudorapidity $1.5 < \eta < 3$ and transverse momentum $p_T > 0.2$ GeV/c comprise the T- sub-event. The T+ sub-event consists of positively charged particles in following kinematic region: $2 < \eta < 3$ and $p_T > 0.2$ GeV/c.

Resolution correction factor was calculated for 3 spectator symmetry planes F1, F2, and F3 using the three sub-event method (for F2 four sub-event technique was employed as well) using the Equation 28 (and for four sub-events Equation 29). Figure 39 shows the centrality dependence of the resolution correction factors R_1 for sub-event symmetry planes F1, F2 and F3 from left to right. For each symmetry plane R_1 was estimated using 3 combinations of sub-events (as indicated in the figure). One can observe that all three estimations for each symmetry plane are in reasonable agreement. This fact may suggest that the contribution of non-flow correlations in the final values of R_1 is very small.

4) Figure 40 shows the rapidity dependence y_{cm} of directed flow v_1 of protons in in 10-30% central Xe+Cs(I) collisions at 3.8 A GeV. The measurements have been performed with respect to the F1, F2, F3 and combined (F2+F3) symmetry planes. The resulting v_1 values of protons are in a good agreement for the measurements with respect to F2, F3 and combined (F2+F3) symmetry planes. The small difference in resulting v_1 values for the measurements with respect to the F1 plane, can be explained by the small contribution of non-flow effects. In order to get the final results, the measurements of directed flow v_1 have been performed with respect to

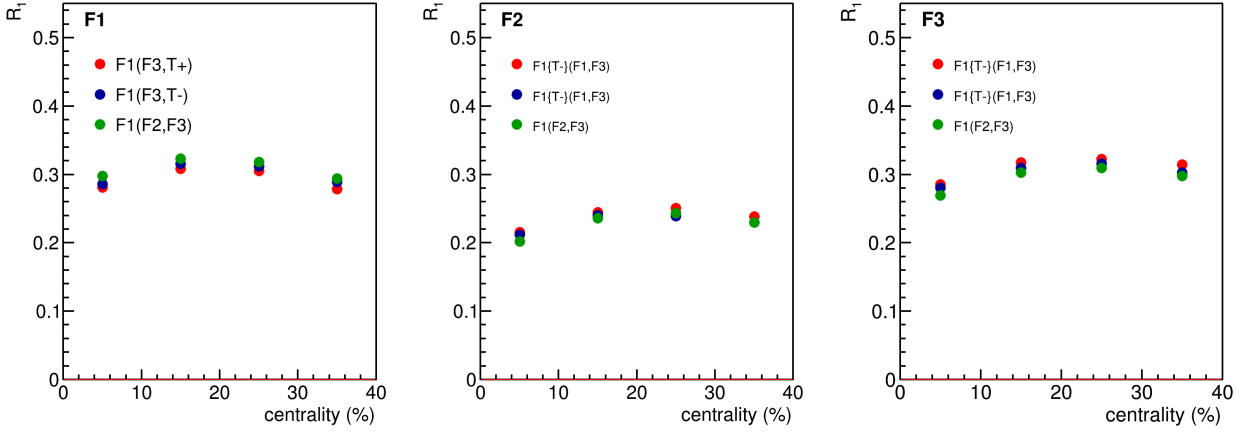


Figure 39: Resolution correction factor R_1 calculated using different combinations as a function of centrality for sub-event symmetry planes F1, F2 and F3 from left to right.

the combined (F2+F3) symmetry plane, see Figure 47.

4.4 Systematic uncertainties of v_1 measurements

In order to estimate systematic uncertainties of v_1 measurements, the following sources were considered:

- Uncertainty in proton momentum reconstruction. We varied the number of stations N_{hits} in inner tracking system used for track reconstruction as well as the values of track χ^2/NDF quality, see results in Figure 42. The overall systematic uncertainty is found to be below 2-5%.
- Contribution from the secondary particles. We studied the difference in v_1 results for tracks with different Distance of the Closest Approach (DCA) to the primary vertex, see the left panel of Figure 43 for results. It is found that proton v_1 values obtained with different DCA cut are in agreement within 1-2%.
- Contamination from the different particle species. We varied the identification selection criteria for protons, see the right panel of Figure 43 for results. Observed is the systematic uncertainty is below 2-4%.

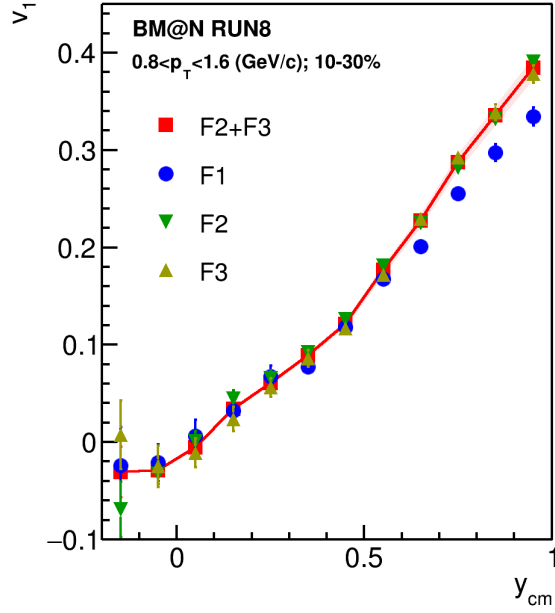


Figure 40: Directed flow v_1 of protons as a function of rapidity y_{cm} measured with respect to different spectator symmetry planes: F1, F2, F3 and combined (F2+F3), see text for the details.

- Contribution due to off-target collisions. We divided the events based on the azimuthal angle of the vertex position and compared the v_1 of protons in each group of events, see results in Figure 44. Systematic variation stays below 5%.
- Acceptance and efficiency. We perform the v_1 flow measurements for protons detected in TOF-400 and TOF-700 separately. We perform the measurements with and without the applying the efficiency correction for protons based on MC simulations for run8, see Figure 45 for results. The results are in a good agreement and we can conclude that the mean value of transverse momentum p_T is not shifted in this rapidity range.
- Run-by-run systematics was estimated dividing the events into several run periods and comparing the results in each group, see the left panel of Figure 46 for results. The systematic uncertainty is less than 5% and found to be less than statistical.

Systematic uncertainties were calculated by the square root of quadratic sum of uncertainties from each source.

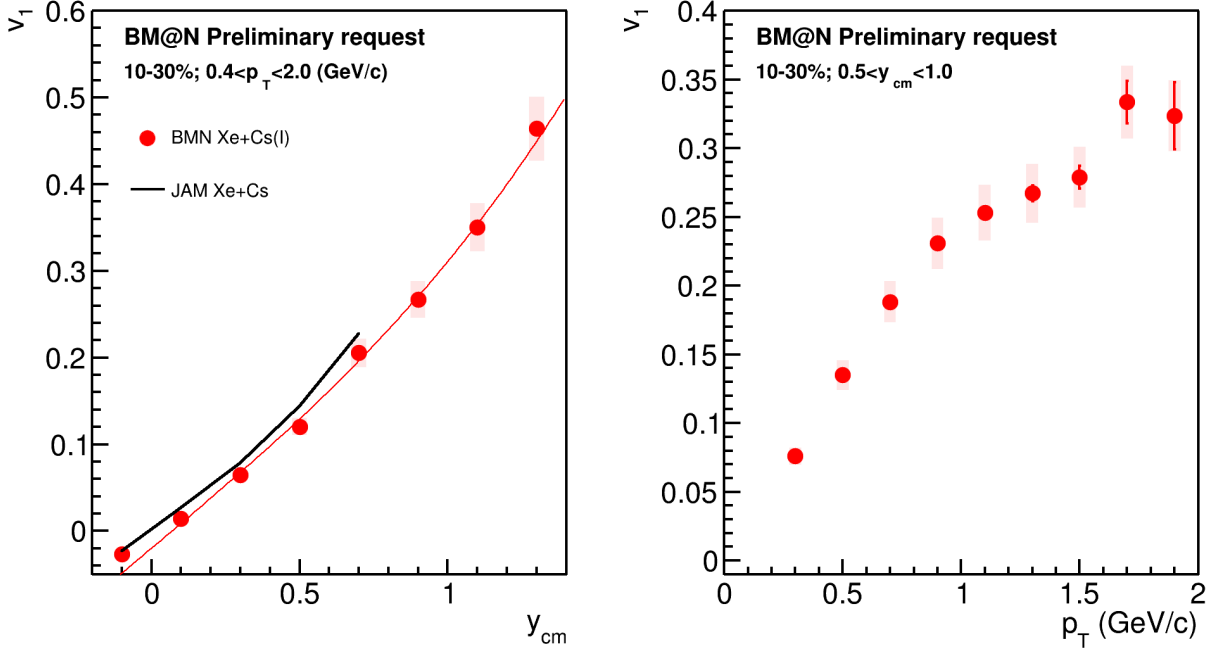


Figure 41: Directed flow v_1 of protons in 10-30% central Xe+Cs(I) collisions at 3.8 A GeV as a function of rapidity y_{cm} (left panel) and transverse momentum p_T (right panel).

5 Results of the directed flow measurements

Directed flow v_1 of protons was measured in 10-30% central Xe+Cs(I) collisions at 3.8 AGeV as a function of rapidity y_{cm} and transverse momentum p_T , see Figure. 47. Rapidity-dependence of v_1 of protons from the experimental data has been compared with predictions from the model JAM transport model [26; 27] with momentum dependent mean field[17; 21]. JAM model roughly captures the overall magnitude and trend of the measured $v_1(y_{cm})$ signal of protons, see black solid line in Figure. 47. The slope of the directed flow v_1 at midrapidity $dv_1/dy_{cm}|_{y_{cm}=0}$ is extracted by fitting the $v_1(y_{cm})$ with polynomial function $v_1 = a + by_{cm} + cy_{cm}^3$ as it was done in other experiments [9; 10; 12; 19].

The slope of v_1 of protons at midrapidity $dv_1/dy_{cm}|_{y_{cm}=0}$ as a function of collision energy is presented in the fig. 48. The results for the BM@N experiment are compared with existing data from other experiments [9; 12; 19]. Directed flow slope at midrapidity $dv_1/dy_{cm}|_{y_{cm}=0}$ are found to be in a reasonable agreement with the existing measurements.

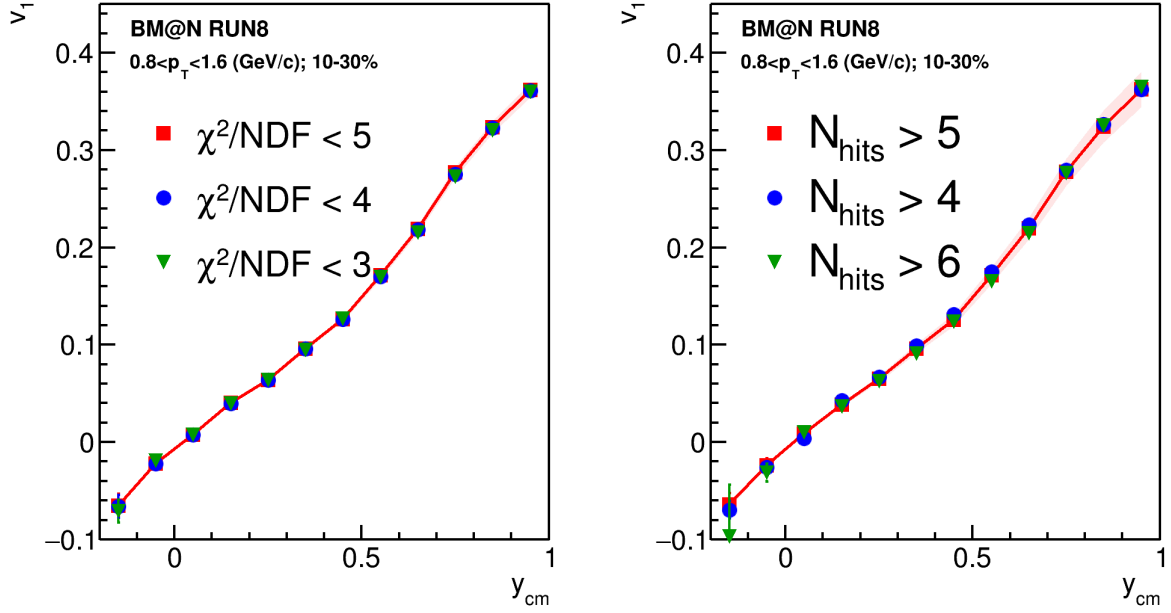


Figure 42: Directed flow v_1 of protons as a function of rapidity y_{cm} measured for different values of the track χ^2/NDF quality (left) and the number of stations used for track reconstruction N_{hits} (right).

References

1. *Sorensen A.* [et al.]. Dense nuclear matter equation of state from heavy-ion collisions // Prog. Part. Nucl. Phys. — 2024. — Vol. 134. — P. 104080.
2. *Poskanzer A. M., Voloshin S. A.* Methods for analyzing anisotropic flow in relativistic nuclear collisions // Phys. Rev. C. — 1998. — Vol. 58. — P. 1671–1678.
3. *Voloshin S., Zhang Y.* Flow study in relativistic nuclear collisions by Fourier expansion of azimuthal particle distributions // Zeitschrift für Physik C Particles and Fields. — 1996. — May. — Vol. 70, no. 4. — P. 665–671.
4. *Voloshin S. A., Poskanzer A. M., Snellings R.* Collective phenomena in non-central nuclear collisions // Landolt-Bornstein / ed. by R. Stock. — 2010. — Vol. 23. — P. 293–333. — arXiv: 0809.2949 [nucl-ex].
5. *Selyuzhenkov I., Voloshin S.* Effects of non-uniform acceptance in anisotropic flow measurement // Phys. Rev. C. — 2008. — Vol. 77. — P. 034904.

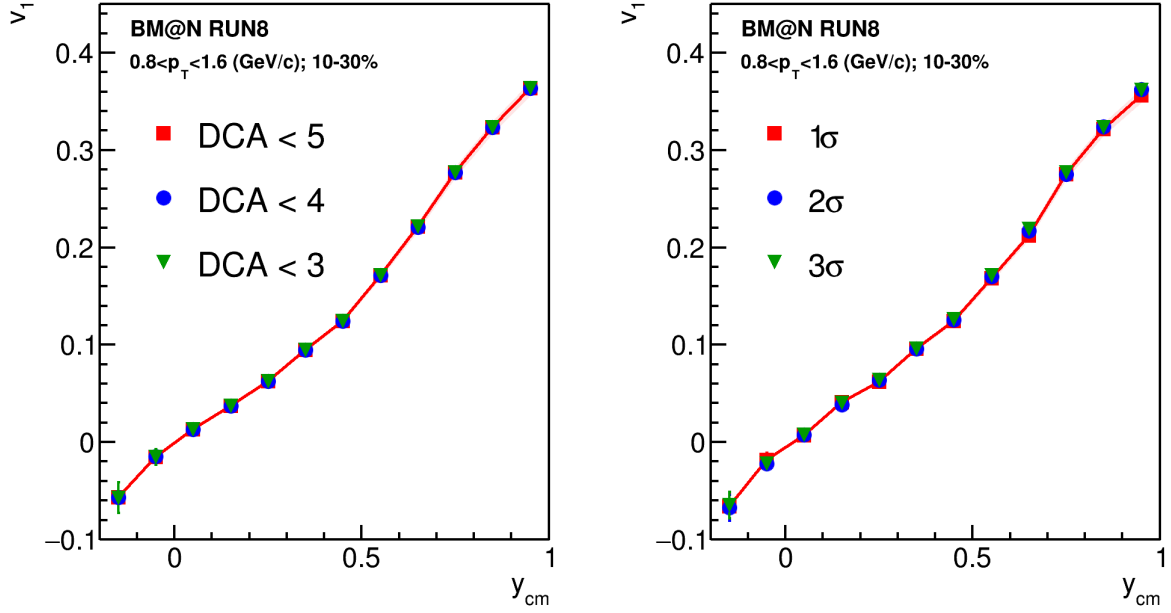


Figure 43: Directed flow v_1 of protons as a function of rapidity y_{cm} measured for different values of the DCA cut and different $n\text{-}\sigma$ PID cuts for the proton identification: $(m^2 - \langle m_p^2 \rangle) < 1, 2, 3 \sigma_{m_p^2}$ cut (right).

6. *Liu H.* [et al.]. Sideward flow in Au + Au collisions between 2-A-GeV and 8-A-GeV // Phys. Rev. Lett. — 2000. — Vol. 84. — P. 5488–5492.
7. *Pinckenburg C.* [et al.]. Elliptic flow: Transition from out-of-plane to in-plane emission in Au + Au collisions // Phys. Rev. Lett. — 1999. — Vol. 83. — P. 1295–1298.
8. *Chung P.* [et al.]. Differential elliptic flow in 2-A-GeV - 6-A-GeV Au+Au collisions: A New constraint for the nuclear equation of state // Phys. Rev. C. — 2002. — Vol. 66. — P. 021901.
9. *Reisdorf W.* [et al.]. Systematics of azimuthal asymmetries in heavy ion collisions in the 1 A GeV regime // Nucl. Phys. A. — 2012. — Vol. 876. — P. 1–60.
10. *Adamczewski-Musch J.* [et al.]. Proton, deuteron and triton flow measurements in Au+Au collisions at $\sqrt{s_{NN}} = 2.4$ GeV // Eur. Phys. J. A. — 2023. — Vol. 59, no. 4. — P. 80.

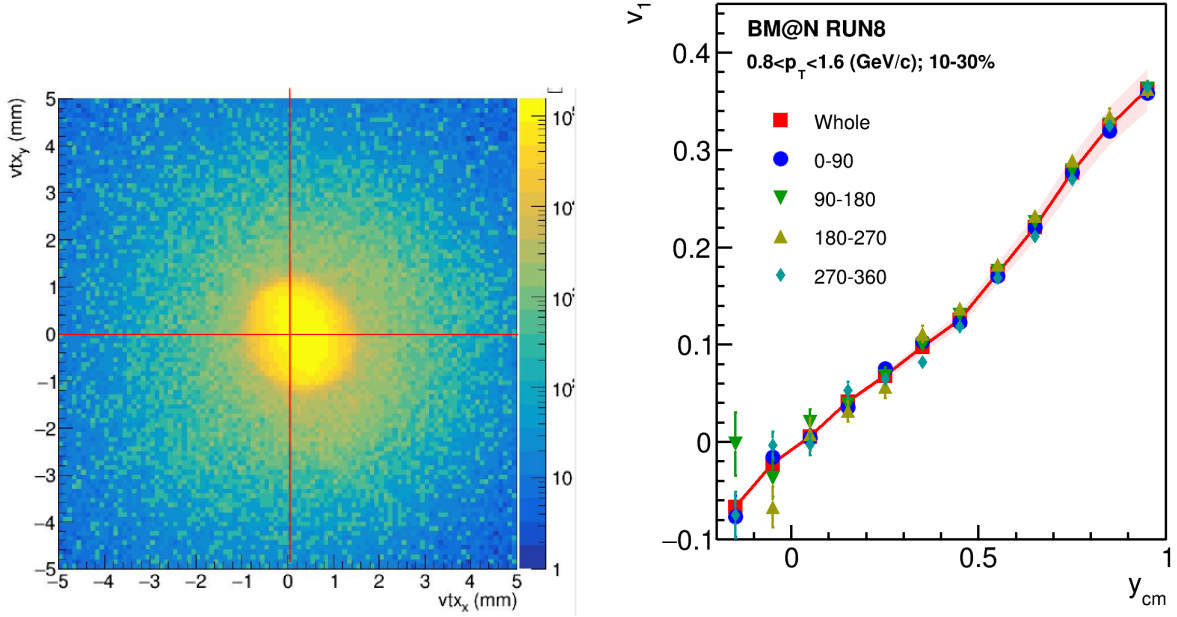


Figure 44: Left: the distribution of the primary vertex in X-Y plane. Right: Directed flow v_1 of protons as a function of rapidity y_{cm} calculated with varying the reconstructed primary vertex position of the collision.

11. *Adam J.* [et al.]. Flow and interferometry results from Au+Au collisions at $\sqrt{s_{NN}} = 4.5$ GeV // Phys. Rev. C. — 2021. — Vol. 103, no. 3. — P. 034908.
12. *Abdallah M. S.* [et al.]. Disappearance of partonic collectivity in $\sqrt{s_{NN}} = 3$ GeV Au+Au collisions at RHIC // Phys. Lett. B. — 2022. — Vol. 827. — P. 137003.
13. *Danielewicz P., Lacey R., Lynch W. G.* Determination of the equation of state of dense matter // Science. — 2002. — Vol. 298. — P. 1592–1596.
14. *Senger P.* Heavy-Ion Collisions at FAIR-NICA Energies // Particles. — 2021. — Vol. 4, no. 2. — P. 214–226.
15. *Le Fèvre A.* [et al.]. Constraining the nuclear matter equation of state around twice saturation density // Nucl. Phys. A. — 2016. — Vol. 945. — P. 112–133.
16. *Oliinychenko D.* [et al.]. Sensitivity of Au+Au collisions to the symmetric nuclear matter equation of state at 2–5 nuclear saturation densities // Phys. Rev. C. — 2023. — Vol. 108, no. 3. — P. 034908. — arXiv: 2208.11996 [nucl-th].

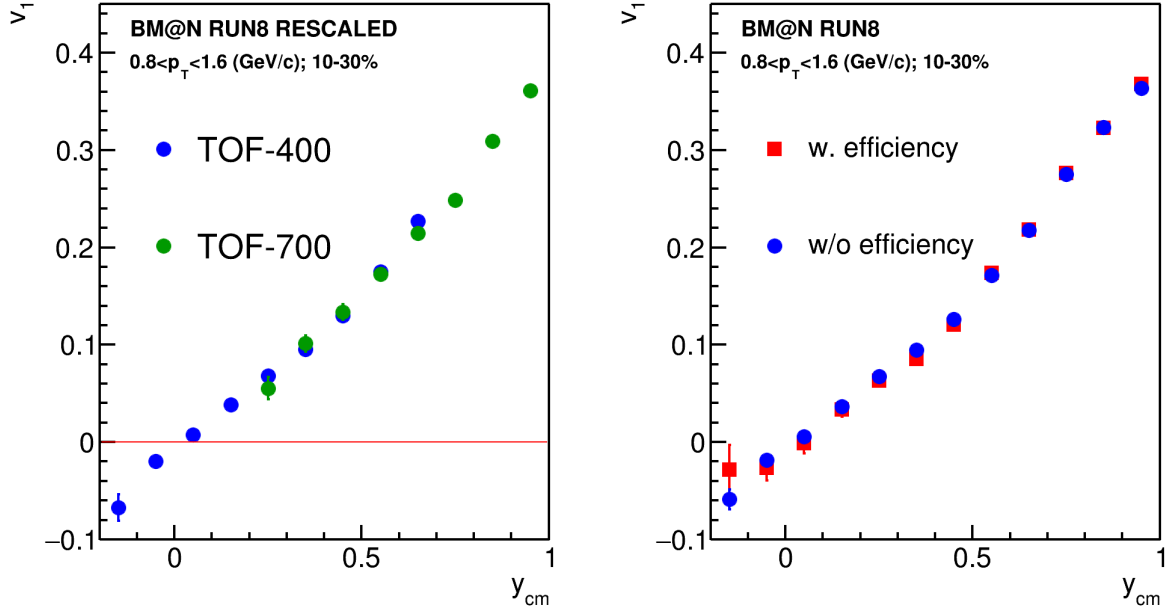


Figure 45: Directed flow v_1 of protons as a function of rapidity y_{cm} measured for protons identified using different TOF-systems (left) and protons weighted and not weighted with efficiency based on MC simulations for run8 (right).

17. *Mamaev M., Taranenko A.* Toward the System Size Dependence of Anisotropic Flow in Heavy-Ion Collisions at $\sqrt{s_{NN}} = 2\text{--}5$ GeV // *Particles*. — 2023. — Vol. 6, no. 2. — P. 622–637.
18. *Afanasiev S. [et al.].* The BM@N spectrometer at the NICA accelerator complex. — 2023. — Dec. — arXiv: 2312.17573 [hep-ex].
19. *Sharma S. R.* First-Order Event Plane Correlated Directed and Triangular Flow from Fixed-Target Energies at RHIC-STAR // *Universe*. — 2024. — Vol. 10, no. 3. — P. 118.
20. *Liu Z.* Anisotropic Flow of Identified Particles in Au + Au Collisions at $\sqrt{s_{NN}} = 3\text{--}3.9$ GeV at RHIC. — 2023. — Dec. — arXiv: 2312.16758 [nucl-ex].
21. *Parfenov P.* Model Study of the Energy Dependence of Anisotropic Flow in Heavy-Ion Collisions at $\sqrt{s_{NN}} = 2\text{--}4.5$ GeV // *Particles*. — 2022. — Vol. 5, no. 4. — P. 561–579.

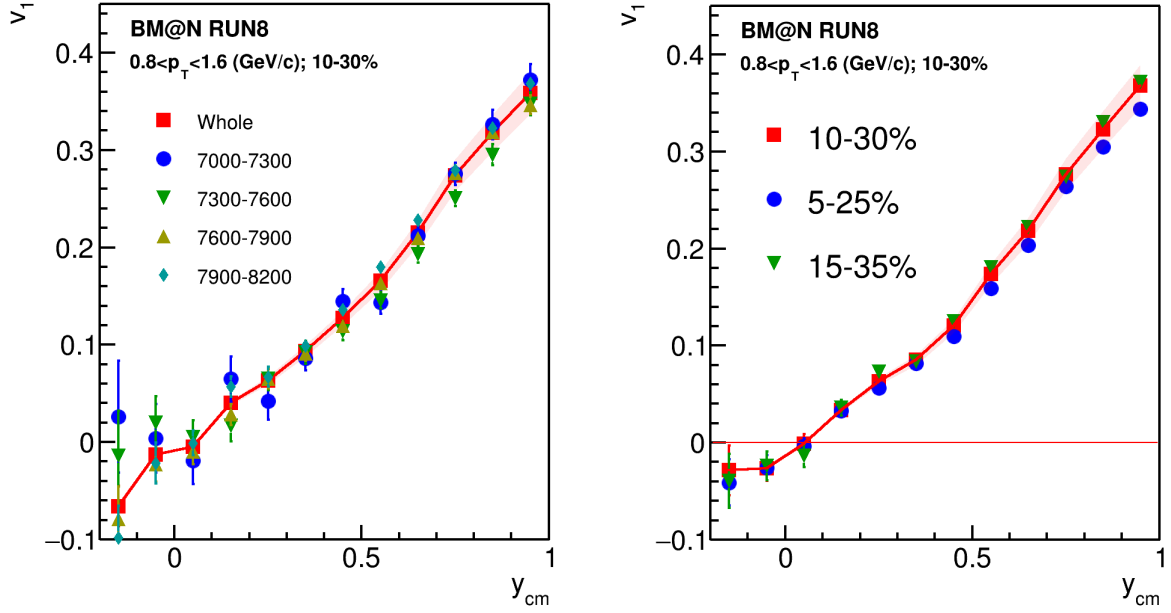


Figure 46: Directed flow v_1 of protons as a function of rapidity y_{cm} measured in the different run periods (left) and for different bins in collision centrality (right).

22. *Larionov A. B.* [et al.]. Squeezeout of nuclear matter in peripheral heavy ion collisions and momentum dependent effective interactions // *Phys. Rev. C.* — 2000. — Vol. 62. — P. 064611.
23. *Bass S. A.* [et al.]. Microscopic models for ultrarelativistic heavy ion collisions // *Prog. Part. Nucl. Phys.* — 1998. — Vol. 41. — P. 255–369.
24. *Aichelin J.* [et al.]. Parton-hadron-quantum-molecular dynamics: A novel microscopic n -body transport approach for heavy-ion collisions, dynamical cluster formation, and hypernuclei production // *Phys. Rev. C.* — 2020. — Vol. 101, no. 4. — P. 044905.
25. *Baznat M.* [et al.]. Monte-Carlo Generator of Heavy Ion Collisions DCM-SMM // *Phys. Part. Nucl. Lett.* — 2020. — Vol. 17, no. 3. — P. 303–324.
26. *Nara Y.* JAM: an event generator for high energy nuclear collisions // *EPJ Web Conf.* / ed. by B. Pattison [et al.]. — 2019. — Vol. 208. — P. 11004.
27. *Nara Y., Ohnishi A.* Mean-field update in the JAM microscopic transport model: Mean-field effects on collective flow in high-energy heavy-ion collisions

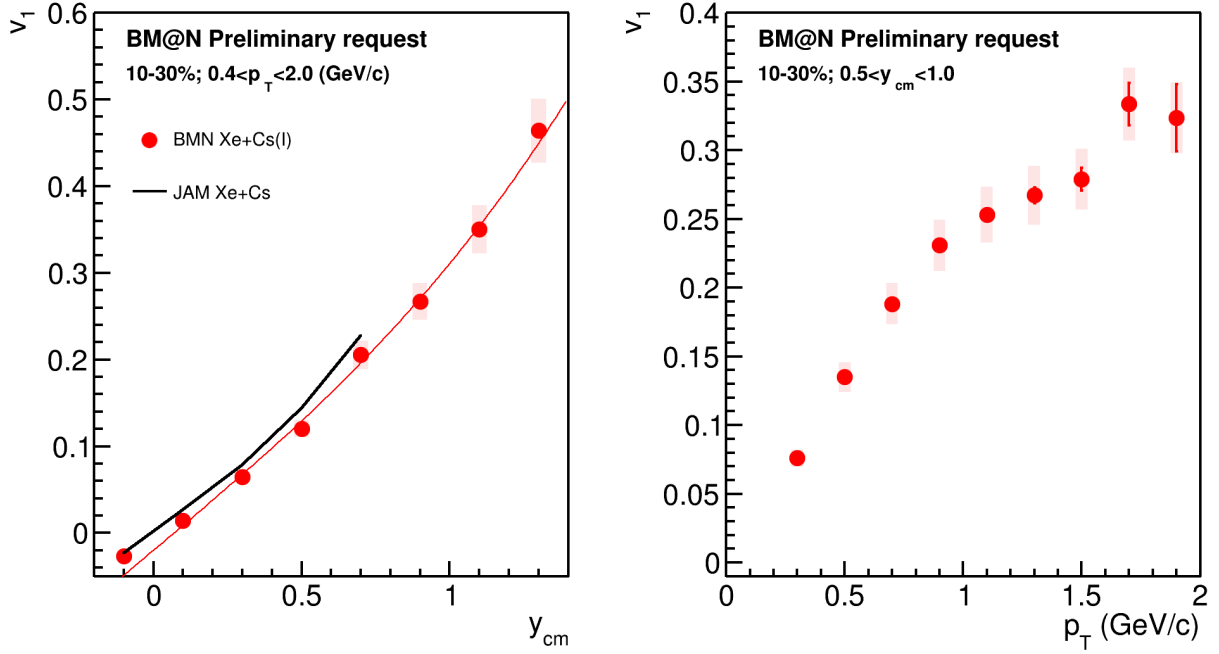


Figure 47: Directed flow v_1 of protons in 10-30% central Xe+Cs(I) collisions at 3.8 A GeV as a function of rapidity y_{cm} (left panel) and transverse momentum p_T (right panel).

at $\sqrt{s_{NN}} = 2 - 20$ GeV energies // Phys. Rev. C. — 2022. — Vol. 105, no. 1. — P. 014911.

28. *Nara Y., Maruyama T., Stoecker H.* Momentum-dependent potential and collective flows within the relativistic quantum molecular dynamics approach based on relativistic mean-field theory // Phys. Rev. C. — 2020. — Vol. 102, no. 2. — P. 024913.
29. *Loizides C., Nagle J., Steinberg P.* Improved version of the PHOBOS Glauber Monte Carlo // SoftwareX. — 2015. — Vol. 1/2. — P. 13–18.
30. *Abelev B. [et al.].* Centrality determination of Pb-Pb collisions at $\sqrt{s_{NN}} = 2.76$ TeV with ALICE // Phys. Rev. C. — 2013. — Vol. 88, no. 4. — P. 044909.
31. *Segal I. [et al.].* Using multiplicity of produced particles for centrality determination in heavy-ion collisions with the CBM experiment // J. Phys. Conf. Ser. / ed. by P. Teterin. — 2020. — Vol. 1690, no. 1. — P. 012107.

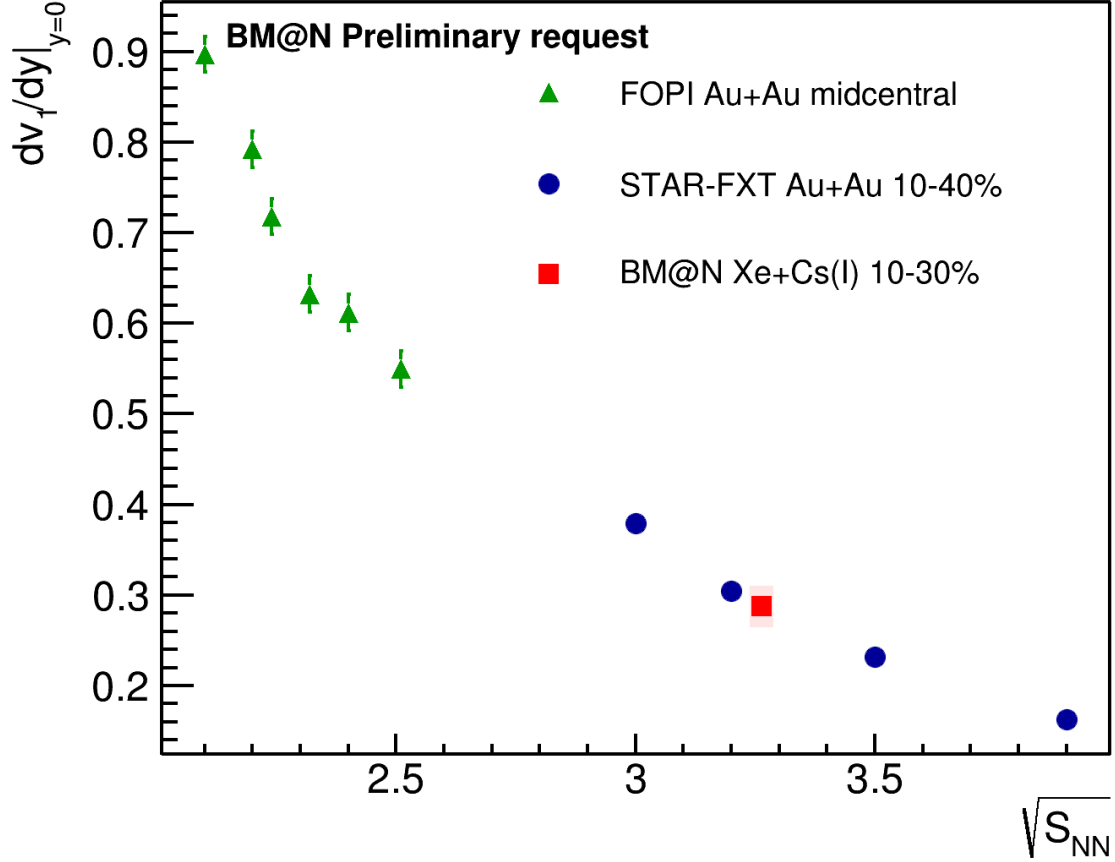


Figure 48: The slope of v_1 of protons at midrapidity $dv_1/dy_{cm}|_{y_{cm}=0}$ as a function of collision energy. The obtained BM@N results were compared with existing data from other experiments [9; 12; 19].

32. *Adamczewski-Musch J.* [et al.]. Centrality determination of Au + Au collisions at 1.23A GeV with HADES // Eur. Phys. J. A. — 2018. — Vol. 54, no. 5. — P. 85.
33. *Tarafdar S., Citron Z., Milov A.* A Centrality Detector Concept // Nucl. Instrum. Meth. A. — 2014. — Vol. 768. — P. 170–178.
34. *Rogly R., Giacalone G., Ollitrault J.-Y.* Reconstructing the impact parameter of proton-nucleus and nucleus-nucleus collisions // Phys. Rev. C. — 2018. — Vol. 98, no. 2. — P. 024902.
35. *Frankland J. D.* [et al.]. Model independent reconstruction of impact parameter distributions for intermediate energy heavy ion collisions // Phys. Rev. C. — 2021. — Vol. 104, no. 3. — P. 034609.

36. *Parfenov P.* [et al.]. Relating Charged Particle Multiplicity to Impact Parameter in Heavy-Ion Collisions at NICA Energies // *Particles*. — 2021. — Vol. 4, no. 2. — P. 275–287.
37. *Idrisov D., Parfenov P., Taranenko A.* Centrality Selection Effect on Elliptic Flow Measurements in Relativistic Heavy-Ion Collisions at NICA Energies // *Particles*. — 2023. — Vol. 6, no. 2. — P. 497–514.
38. *Selyuzhenkov I., Kreis L.* QnTools -A framework for multi-differential acceptance correction and anisotropic flow analysis // <https://github.com/HeavyIonAnalysis/QnTools> 2024.